



# Sn(II) chloride speciation and equilibrium Sn isotope fractionation under hydrothermal conditions: A first principles study

Tianhua Wang<sup>1</sup>, Jia-Xin She<sup>1</sup>, Kun Yin, Kai Wang, Yingjie Zhang, Xiancai Lu, Xiandong Liu<sup>\*</sup>, Weiqiang Li<sup>\*</sup>

*State Key Laboratory for Mineral Deposits Research, School of Earth Sciences and Engineering, Nanjing University, Nanjing, Jiangsu 210023, China*

Received 4 September 2020; accepted in revised form 15 February 2021; available online 24 February 2021

## Abstract

Knowledge of Sn(II) speciation in aqueous and gaseous phases and the corresponding isotope effects are critical for understanding the transport and deposition of Sn in various geological and cosmochemical processes. In this study, we use first principles method to investigate the speciation of stannous (Sn(II)) chloride in fluids under hydrothermal and supercritical conditions. The results show that  $\text{SnCl}_3^-$ ,  $\text{SnCl}_2(\text{H}_2\text{O})$  and  $\text{SnCl}(\text{H}_2\text{O})_2^+$  are stable in hydrothermal solutions at temperatures of up to 300 °C, with  $\text{SnCl}_3^-$  being the dominant species, whereas  $\text{SnCl}_2$  and  $\text{SnCl}_2(\text{H}_2\text{O})$  are the stable species in vapor phases. Notably,  $\text{SnCl}_2$  is found to be stable under supercritical conditions. The reduced partition function ratios ( $\beta$  factors) for the stable Sn(II) species and three major Sn minerals (cassiterite, megawite, and romarchite) are also calculated by first principles methods. The calculation results show that under equilibrium, heavy Sn isotopes are preferentially partitioned into stannic (Sn(IV)) species, and gaseous species enrich heavy Sn isotopes relative to aqueous species. Based on the equilibrium Sn isotope fractionation factors derived in this study, we use a transport-precipitation model to evaluate the Sn isotope response to cassiterite precipitation in hydrothermal fluids. The modeling results show that significant Sn isotope variability could be produced during cassiterite precipitation, with temperature and Sn speciation being the primary controlling factors. Furthermore, by comparing the Sn isotope variability in natural cassiterite and those derived from the model, we argue that Sn should occur predominantly as Sn(IV) species in hydrothermal fluids during cassiterite precipitation in tin mineralizing systems.

© 2021 Elsevier Ltd. All rights reserved.

**Keywords:** Tin; Hydrothermal fluids; Speciation; Equilibrium isotope fractionation; First principles molecular dynamics (FPMD); First principles calculation

## 1. INTRODUCTION

Tin (Sn) is recognized as a strategic critical metal because of its vital roles in many emerging industries such

as clean energy and electronics (Hayes and McCullough, 2018; Tarselli, 2017). Tin is a volatile trace element with three oxidation states (i.e., 0, +2 and +4), and thus its geochemical behavior can be strongly influenced by redox con-

<sup>\*</sup> Corresponding authors.

E-mail addresses: [xiandongliu@gmail.com](mailto:xiandongliu@gmail.com) (X. Liu), [liweiqiang@nju.edu.cn](mailto:liweiqiang@nju.edu.cn) (W. Li).

<sup>1</sup> The two authors contributed equally to this work.

ditions (Chen et al., 2000; Teng et al., 2017). For example, tin is an incompatible element during magmatic processes and there may be difference between the incompatibility of  $\text{Sn}^{4+}$  and  $\text{Sn}^{2+}$  (e.g., Farges et al., 2006; Badullovich et al., 2017). Redox conditions also have strong effect on the solubility of cassiterite in hydrothermal fluids or silicate melts (e.g., Jackson and Helgeson, 1985; Bhalla et al., 2005). Tin has ten stable isotopes (i.e.,  $^{112}\text{Sn}$ ,  $^{114}\text{Sn}$ ,  $^{115}\text{Sn}$ ,  $^{116}\text{Sn}$ ,  $^{117}\text{Sn}$ ,  $^{118}\text{Sn}$ ,  $^{119}\text{Sn}$ ,  $^{120}\text{Sn}$ ,  $^{122}\text{Sn}$  and  $^{124}\text{Sn}$ ) and its isotope geochemistry has aroused great interest in recent years for its applications in probing planetary processes (Creech and Moynier, 2019; Wang et al., 2019b), magmatic and hydrothermal processes (Badullovich et al., 2017; Wang et al., 2018; Yao et al., 2018; Roskosz et al., 2020), environmental processes (Malinovskiy et al., 2009) and archaeological problems (Balliana et al., 2013; Mason et al., 2016, 2020).

Mineralization of Sn is primarily associated with hydrothermal processes (Heinrich, 1990; Lehmann, 1990; Chen et al., 2000). Therefore, knowledge of speciation of Sn in geological fluids is crucial for understanding its deposition mechanisms. Speciation of Sn in hydrothermal fluids has been studied using various methods but it remained a topic of hot debate. Stability of Sn(IV) species in aqueous solutions has been reported based on data of *in situ* extended X-ray absorption fine structure (EXAFS) spectroscopy (Sherman et al., 2000), Raman spectroscopy (Schmidt, 2018) and first principles molecular dynamics (FPMD) simulations (She et al., 2020), however, numerous solubility experiments have indicated that Sn(II) chloride is most likely to be responsible for the transport of Sn in hydrothermal fluids (e.g., Pabalan, 1986; Wilson and Eugster, 1990; Taylor and Wall, 1993; Duc-Tin et al., 2007). Furthermore, the exact speciation of Sn(II) chloride remains unclear. Solubility experiments at 200–350 °C by Pabalan (1986) emphasized the dominance of  $\text{SnCl}_4^{2-}$  and  $\text{SnCl}_3^-$ . Similarly, Sherman et al. (2000) suggested that the Sn(II)—Cl coordination numbers increased from 3.4 at 25 °C to about 4.0 at 350 °C, and attributed it to the enhanced stability of  $\text{SnCl}_4^{2-}$  at higher temperature. In contrast, in an *in situ* ultraviolet (UV) spectroscopy study, Müller and Seward (2001) only detected the presence of  $\text{SnCl}_4^{2-}$  at  $T \leq 150$  °C, and proposed that  $\text{SnCl}_3^-$  and  $\text{SnCl}_2$  were the dominant Sn(II) chlorides at higher temperatures up to 300 °C. In a recent *in situ* Raman spectroscopy study on cassiterite dissolved in HCl solutions,  $\text{SnCl}_3^-$  was thought to be the only detectable Sn(II) species (Schmidt, 2018). The FPMD simulations by Sherman (2010) indicated that  $\text{SnCl}_3^-$  and  $\text{SnCl}_2$  coexisted at 25 °C and  $\text{SnCl}_3^-$  was dominant at 325 °C, whereas  $\text{SnCl}_4^{2-}$  was not stable. However, no detailed structural or thermodynamic information was provided by Sherman (2010). In supercritical aqueous fluids,  $\text{SnCl}_2$  was proposed as the common dominant species based on solubility experiments from 400 °C to 800 °C (Wilson and Eugster, 1990; Taylor and Wall, 1993; Duc-Tin et al., 2007).

The poor understanding of Sn speciation in various kinds of fluids is also a main obstacle for applying Sn isotopes to many systems. Existing studies demonstrated that Sn isotope fractionation takes place during crystallization

fractionation (Badullovich et al., 2017), partial melting (Wang et al., 2018), redox reactions (Yao et al., 2018; Wang et al., 2019a) and liquid–vapor partitioning (Wang et al., 2019a; She et al., 2020). The diversity of the bonding environments of Sn in various geological materials (e.g., Sherman et al., 2000; Polyakov et al., 2005; Roskosz et al., 2020) is likely the main reason for causing Sn isotope fractionation (Badullovich et al., 2017; Yao et al., 2018; Wang et al., 2019b; Qu et al., 2020). However, Sn isotope fractionation factor data are available for only a very limited number of Sn-bearing solids (Polyakov et al., 2005) and molecules (She et al., 2020). No experimental isotope fractionation factor for Sn(II) species has been reported due to the tendency of Sn(II) oxidation at ambient conditions (Wang et al., 2019a). Additional challenges in experimental approaches include the difficulty in separating aqueous Sn(II) and Sn(IV) (Altunay and Gürkan, 2015). Detailed knowledge of Sn speciation in geological fluids and corresponding fractionation factors are necessary for interpreting Sn isotope data from natural samples (Yao et al., 2018; Qu et al., 2020).

First principles molecular dynamics (FPMD) simulation has proven powerful for investigating the coordination chemistry of metal elements in hydrothermal fluids (see the reviews in Brugger et al., 2016; Pokrovski et al., 2013a) and magmas (e.g., Wagner et al., 2017a,b; Wang et al., 2020). First principles modelling has been applied to aqueous chloride species of many metal ions, such as copper (Sherman, 2007, 2010; Mei et al., 2013, 2014), silver (Liu et al., 2012; Pokrovski et al., 2013b), high field strength elements (HFSE) (Jahn et al., 2015) and rare earth elements (REE) (Stefanski and Jahn, 2020; Guan et al., 2020). First principles calculation is also a powerful method to derive equilibrium isotope fractionation factors that are relevant to geological problems (see the reviews in Blanchard et al., 2017; Schauble, 2004), including aqueous/gaseous species (e.g., Liu and Tossell, 2005; Rustad et al., 2008; Hill and Schauble, 2008; Li et al., 2009) and minerals (e.g., Schauble, 2011; Huang et al., 2013; Wu et al., 2015b; Méheut et al., 2021). In our earlier study, by using first principles calculation, we evaluated the stability of possible Sn(IV) chloride species and calculated the equilibrium isotope fractionation factors of the stable Sn(IV) chloride species (She et al., 2020).

In this study, we applied first principles methods to constrain the speciation of Sn(II) chloride in fluids under hydrothermal conditions, and to calculate equilibrium Sn isotope fractionation factors between aqueous, vapor, supercritical fluids, and three major Sn-bearing minerals. The calculation results provide basic constraints for understanding hydrothermal Sn mineralization and interpretation of the rapidly growing Sn isotope data from Sn mineral deposits.

## 2. METHODOLOGY

The workflow of this study is as follows. We firstly used free energy calculations to constrain the stability of the dominant Sn(II) species under hydrothermal conditions. Based on these results, we calculated the reduced partition

function ratios ( $\beta$  factors) for the stable Sn(II) species based on the vibrational frequencies derived with static first principles calculations. Reduced partition function ratios ( $\beta$  factors) of cassiterite ( $\text{SnO}_2$ ), megawite ( $\text{CaSnO}_3$ ), and romarchite ( $\text{SnO}$ ) were also calculated using static first principles methods. These  $\beta$  factors were used to derive equilibrium Sn isotope fractionation factors between different fluids and minerals, which were then coupled to a transport-precipitation model for discussion of Sn isotope fractionation during the hydrothermal ore-forming processes. The details of the calculation methods in this study are shown as below.

## 2.1. First principles molecular dynamics (FPMD)

### 2.1.1. Models

The systems of FPMD simulations are listed in Table 1. The simulation cells were cubic boxes with 3D periodic boundary conditions with a side length of 12.43 Å. The numbers of water molecules were estimated from the equation of state of water for each temperature and the corresponding saturated vapor pressure ( $P_{\text{sat}}$ ) (for aqueous solutions at 330–573 K) or 1.5 kbar (for supercritical aqueous fluids at 773 K and 973 K) (Wagner et al., 2000; Zhang and Duan, 2005). The temperature of 330 K was set for the ambient conditions to avoid the glassy behavior of liquid water at lower temperatures (VandeVondele et al., 2005a).

### 2.1.2. Method of constraint

To determine the stability of Sn(II)—Cl complexes in aqueous solutions, the free energy changes of the relevant dissociation reactions (i.e., from  $\text{SnCl}_4^{2-}/\text{SnCl}_3^-/\text{SnCl}_2/\text{SnCl}^+$  to  $\text{SnCl}_3^-/\text{SnCl}_2/\text{SnCl}^+/\text{Sn}^{2+}$ ) were computed by a series of constrained FPMD simulations. The free energy change ( $\Delta F$ ) was obtained by integrating the mean force ( $f$ ) along a reaction coordinate ( $Q$ ) (Carter et al., 1989; Sprik and Ciccotti, 1998):

$$\Delta F(Q) = - \int_{Q_0}^Q dQ' f(Q') \quad (1)$$

The distance between one  $\text{Cl}^-$  and  $\text{Sn}^{2+}$  was chosen as the reaction coordinate ( $Q$ ) in the simulations.

### 2.1.3. Computational details

FPMD simulations were performed with the CP2K/QUICKSTEP package (Kühne et al., 2020; Hutter et al., 2014; VandeVondele et al., 2005b). In this package, density functional theory (DFT) is implemented with the mixed Gaussian and plane waves (GPW) method (Lippert et al., 1997). PBE (Perdew-Burke-Ernzerhof) exchange–correlation functional (Perdew et al., 1996), D3 dispersion correction (Grimme et al., 2010), double zeta valence polarizable (DZVP) basis sets (VandeVondele and Hutter, 2007) and GTH (Goedecker-Teter-Hutter) pseudopotentials (Goedecker et al., 1996) were employed. The cutoff of the electronic density was set to be 400 Ry. The wave function optimization tolerance was set to be  $10^{-6}$ . All FPMD simulations were performed in canonical (NVT) ensemble with a time step of 0.5 fs. Except for the simulations of  $\text{SnCl}_4^{2-}$  (see below), each production simulation was performed for over 30.0 ps, following a prior equilibration for over 5.0 ps. The temperatures were controlled with the Nosé-Hoover chain thermostat (Nosé, 1984a,b; Hoover, 1985).

For the equilibration of  $\text{SnCl}_4^{2-}$ , the four Sn—Cl bonds were restrained by using harmonic potentials to avoid the rapid spontaneous dissociation of the complex. The Sn—Cl equilibrium distance was set to 2.47 Å, based on the EXAFS study by Sherman et al. (2000). The restrained simulations were carried out for 10.0 ps. After that the production runs without restraints were performed for at least 60.0 ps at 330 K and 368 K, and for 10.0 ps at 573 K.

## 2.2. Static first principles calculations

### 2.2.1. Models

According to the FPMD simulations in this study,  $\text{SnCl}_3^-$  is the dominant Sn(II)—Cl species in aqueous solutions up to 300 °C, and  $\text{SnCl}_2(\text{H}_2\text{O})$  can coexist with it (see Section 3.1). For the static calculations of aqueous species,  $\text{SnCl}_3^-$  and  $\text{SnCl}_2(\text{H}_2\text{O})$  were modeled with 18 or 24 solvent

Table 1  
Systems of FPMD simulations.

Temperature (K)	Pressure (bar)	System
330 (aqueous)	0.17 ( $P_{\text{sat}}$ )	$\text{SnCl}_4^{2-} + 60 \text{ H}_2\text{O}$ $\text{SnCl}_3^- + 61 \text{ H}_2\text{O}$ $\text{SnCl}_2 + 62 \text{ H}_2\text{O}$ $\text{SnCl}^+ + 63 \text{ H}_2\text{O}$ $\text{Sn}^{2+} + 64 \text{ H}_2\text{O}$
368 (aqueous)	0.84 ( $P_{\text{sat}}$ )	$\text{SnCl}_4^{2-} + 58 \text{ H}_2\text{O}$
573 (aqueous)	85.70 ( $P_{\text{sat}}$ )	$\text{SnCl}_4^{2-} + 44 \text{ H}_2\text{O}$ $\text{SnCl}_3^- + 44 \text{ H}_2\text{O}$ $\text{SnCl}_2 + 45 \text{ H}_2\text{O}$ $\text{SnCl}^+ + 45 \text{ H}_2\text{O}$ $\text{Sn}^{2+} + 46 \text{ H}_2\text{O}$
773 (supercritical)	1500.00	$\text{SnCl}_2 + 40 \text{ H}_2\text{O}$
973 (supercritical)	1500.00	$\text{SnCl}_2 + 25 \text{ H}_2\text{O}$

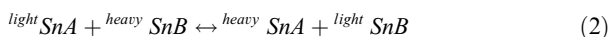
water molecules accounting for the solvation effect. The initial structures of the complexes were derived from the FPMD simulations.

Geological vapors usually have very low dielectric constant, favoring neutral species (Pokrovski et al., 2013a). Therefore, six neutral complexes including  $\text{SnCl}_2$ ,  $\text{SnCl}_2(\text{H}_2\text{O})$ ,  $\text{SnCl}_2(\text{HCl})$ ,  $\text{SnCl}(\text{OH})$ ,  $\text{Sn}(\text{OH})_2$  and  $\text{SnO}$  were selected as the possible gaseous Sn(II) species for calculation.

For Sn-bearing minerals, we focused on cassiterite ( $\text{SnO}_2$ ), megawite ( $\text{CaSnO}_3$ ), and romarchite ( $\text{SnO}$ ), to compare with the results from the nuclear resonant inelastic X-ray scattering (NRIXS) study by Polyakov et al. (2005). The models of cassiterite, megawite, and romarchite were supercells consisting of  $2 \times 2 \times 4$  (96 atoms),  $2 \times 2 \times 2$  (160 atoms), and  $5 \times 5 \times 4$  (400 atoms) unit cells respectively. To evaluate the finite size effects, we also built the  $3 \times 3 \times 5$  supercells (270 atoms) for cassiterite and  $3 \times 3 \times 3$  supercells (540 atoms) for megawite, respectively. Their initial structures were constructed based on neutron diffraction data for cassiterite and romarchite (Bolzan et al., 1997; Pannetier and Denes, 1980) and X-ray diffraction data for megawite (Zhao et al., 2004).

### 2.2.2. Thermodynamic equilibrium isotope fractionation

For the isotope exchange reaction of light Sn isotope  $^{light}\text{Sn}$  and heavy Sn isotope  $^{heavy}\text{Sn}$  in two tin isotopomers  $\text{SnA}$  and  $\text{SnB}$ :



the thermodynamic equilibrium Sn isotope fractionation factor ( $\alpha_{\text{SnA-SnB}}$ ) between  $\text{SnA}$  and  $\text{SnB}$  can be expressed as

$$\alpha_{\text{SnA-SnB}} = \left( \frac{^{heavy}\text{Sn}}{^{light}\text{Sn}} \right)_{\text{SnA}} / \left( \frac{^{heavy}\text{Sn}}{^{light}\text{Sn}} \right)_{\text{SnB}} = \frac{\beta_{\text{SnA}}}{\beta_{\text{SnB}}} \quad (3)$$

where  $\beta_{\text{SnA}}$  and  $\beta_{\text{SnB}}$  are the reduced partition function ratio (RPF) of Sn isotopes in  $\text{SnA}$  and  $\text{SnB}$  respectively. The difference of Sn isotope compositions between  $\text{SnA}$  and  $\text{SnB}$ ,  $\Delta_{\text{SnA-SnB}}$ , can be expressed as

$$\Delta_{\text{SnA-SnB}} \approx 1000 \ln \alpha_{\text{SnA-SnB}} = 1000 \ln \beta_{\text{SnA}} - 1000 \ln \beta_{\text{SnB}} \quad (4)$$

According to the Urey model or Bigeleisen-Mayer equation (Urey, 1947; Bigeleisen and Mayer, 1947), the  $\beta$  factor or RPF can be calculated from the harmonic approximation:

$$\beta_{\text{SnA}} = \text{RPF}_{\text{SnA}} = \prod_{i=1}^N \frac{^{heavy}u_i}{^{light}u_i} \cdot \frac{e^{-\frac{^{heavy}u_i}{2}}}{1 - e^{-^{heavy}u_i}} \cdot \frac{1 - e^{-^{light}u_i}}{e^{-\frac{^{light}u_i}{2}}} \quad (5)$$

with

$$u_i = \frac{hv_i}{k_B T} \quad (6)$$

where  $N = 3n - 6$  or  $3n - 3$ , which denotes the number of harmonic vibrational modes for a non-linear molecule containing  $n$  atoms or the number of phonon modes for a solid system containing  $n$  atoms, respectively.  $h$ ,  $v_i$ ,  $k_B$ , and  $T$  denote the Planck constant, vibrational (phonon) frequency, the Boltzmann constant, and temperature, respectively. In this study, the equilibrium fractionation factors

of  $^{122}\text{Sn}/^{116}\text{Sn}$  among the aqueous and gaseous Sn(II) chlorides and Sn-bearing minerals were calculated.

### 2.2.3. Computational details for aqueous and gaseous species

The static first principles calculations for aqueous and gaseous Sn(II) species were carried out by using the Gaussian 09 package (Frisch et al., 2013). B3LYP hybrid exchange–correlation functional (Becke, 1993; Lee et al., 1988) and def2-TZVP basis sets (Weigend and Ahlrichs, 2005) were employed. Our previous study has shown that with this setting, the calculated bond length of  $\text{SnCl}_4$  was in good agreement with experimentally determined results, and the differences between calculated and observed vibrational frequencies were within 5.4% (She et al., 2020). For comparison, the structures and vibrational frequencies of  $\text{SnCl}_4$  and  $\text{SnCl}_2$  were also calculated with the CCSD(T) method (Raghavachari et al., 1989), which is regarded as the “gold standard” for quantum chemical calculation (Foresman and Frisch, 2015). The aug-cc-pVTZ(-pp)/aug-cc-pVQZ(-pp) basis sets were used for Sn and Cl (Peterson, 2003; Woon and Dunning, 1993). We also compared the calculated bond lengths and vibrational frequencies of Sn(II) species with previous studies (see Table 2 in Section 3.3).

To determine the relative stability of the gaseous species, the Gibbs free energy changes ( $\Delta G$ ) of the reactions in Table 3 in Section 3.3 were calculated with:

$$\Delta G = \sum G_{\text{prod}} - \sum G_{\text{react}} \quad (7)$$

where  $\sum G_{\text{prod}}$  and  $\sum G_{\text{react}}$  are the total Gibbs free energy values of the product and the reactant states, respectively. These quantities were computed with Gaussian (Foresman and Frisch, 2015) following the methods of McQuarrie and Simon (1999).

To evaluate the computational bias of the transport-precipitation model in Section 4.2, we performed additional calculations for  $\text{SnCl}_4$ ,  $\text{cis-SnCl}_4(\text{H}_2\text{O})_2(\text{aq})$  and  $\text{SnCl}_3^-(\text{aq})$  with B3LYP hybrid functional, triple zeta valence polarizable (TZVP) and auxiliary basis sets (VandeVondele and Hutter, 2007; Guidon et al., 2010) and GTH pseudopotentials by using the CP2K/QUICKSTEP package. For  $\text{cis-SnCl}_4(\text{H}_2\text{O})_2(\text{aq})$  and  $\text{SnCl}_3^-(\text{aq})$ , 18 solvent water molecules were added to the model. These calculations were carried out in cubic boxes with a side length of 25.00 Å by using the BFGS (Broyden-Fletcher-Goldfarb-Shanno) algorithm (Byrd et al., 1995). The Martyna-Tuckerman scheme was used to solve the Poisson equation of non-periodic boundary conditions systems (Martyna and Tuckerman, 1999). The cutoff of the electronic density was set to be 1200 Ry, and the wave function optimization tolerance was set to be  $10^{-8}$ .

### 2.2.4. Computational details for Sn-bearing minerals

For Sn-bearing minerals, cell optimization was performed by using the CP2K/QUICKSTEP package, and the phonon frequencies were calculated by combining QUICKSTEP with the Phonopy package (Togo and Tanaka, 2015). We optimized the structure and calculated the  $1000 \ln^{122/116}\beta$  values of cassiterite at different theoretical levels to investigate the effect of exchange–correlation

Table 2  
Key structural parameters of gaseous SnCl<sub>2</sub> and SnO molecules.

Bond length (Å)	Angle (°)	Vibrational frequencies (cm <sup>-1</sup> )			Method
<i>SnCl<sub>2</sub></i> <sup>a</sup>					
2.390	99.6	115.07	328.46	344.74	This study <sup>b</sup>
2.371	97.8	123.18	349.07	364.48	This study <sup>c</sup>
2.352	97.6	125.83	350.14	367.30	This study <sup>d</sup>
2.393	97.7	118	342	358	CCSD(T) <sup>e</sup>
2.362	98.1	121.5	342.6	359.2	CCSD(T) <sup>f</sup>
2.335	99.1	121	333	352	Electron diffraction and spectroscopic analysis <sup>g</sup>
		121	347	355	Raman spectra <sup>h</sup>
<i>SnO</i>					
1.832		845.93			This study
1.899		812			CCSD(T) <sup>i</sup>
1.836		812.3			CCSD(T) <sup>j</sup>
		810			Photoelectron spectra <sup>k</sup>

<sup>a</sup> See Levy et al. (2003) and Lee et al. (2007) for more structure parameters and vibrational frequencies of SnCl<sub>2</sub>.

<sup>b</sup> At the B3LYP/def2-TZVP level.

<sup>c</sup> At the CCSD(T)/aug-cc-pVTZ(-pp) level.

<sup>d</sup> At the CCSD(T)/aug-cc-pVQZ(-pp) level.

<sup>e</sup> Kalugina and Thakkar (2015).

<sup>f</sup> Thanthirawatte et al. (2015).

<sup>g</sup> Ermakov et al. (1991).

<sup>h</sup> Fields et al. (1995).

<sup>i</sup> de Lima Batista et al. (2012).

<sup>j</sup> Wolf et al. (2004). See this article for more structure parameters and vibrational frequencies of SnO.

<sup>k</sup> Davico et al. (2000).

Table 3  
Gibbs free energy changes ( $\Delta G$ ) of the reactions among possible Sn(II) species in vapor phases calculated at the B3LYP/def2-TZVP level.

Reaction	T-P condition (K, bar)	$\Delta G$ (kcal/mol)
SnCl <sub>2</sub> (H <sub>2</sub> O) → SnCl <sub>2</sub> + H <sub>2</sub> O	298.15, 0.03 (P <sub>sat</sub> )	1.71
	573, 85.70 (P <sub>sat</sub> )	0.69
	773, 1500.00	1.20
	973, 1500.00	-1.35
SnCl <sub>2</sub> (HCl) → SnCl <sub>2</sub> + HCl	298.15, 0.03	-6.31
	573, 85.70	-5.64
	773, 1500.00	-3.92
	973, 1500.00	-5.30
SnCl(OH) + HCl → SnCl <sub>2</sub> + H <sub>2</sub> O	298.15, 0.03	-11.86
	573, 85.70	-12.00
	773, 1500.00	-11.97
	973, 1500.00	-11.85
Sn(OH) <sub>2</sub> + 2 HCl → SnCl <sub>2</sub> + 2 H <sub>2</sub> O	298.15, 0.03	-27.40
	573, 85.70	-28.03
	773, 1500.00	-28.23
	973, 1500.00	-28.25
SnO + 2 HCl → SnCl <sub>2</sub> + H <sub>2</sub> O	298.15, 0.03	-60.44
	573, 85.70	-60.32
	773, 1500.00	-61.22
	973, 1500.00	-58.84

functionals and basis sets on the results. In these calculations, LDA (local density approximation) (Goedecker et al., 1996), PBE functional (GGA (generalized gradient approximation) level) and B3LYP hybrid functional were employed, together with DZVP or TZVP basis sets and GTH pseudopotentials. Cell optimization was carried out

by using the BFGS algorithm. The cutoff of the electronic density and the wave function optimization tolerance were set to be 1200 Ry and 10<sup>-8</sup>, respectively.

The optimized lattice parameters of cassiterite (see Table S1 in the supplementary materials) show that there was no obvious difference between the results of DZVP

and TZVP basis sets. With DZVP basis sets, calculation using LDA led to the best match with the experimental lattice parameters (<0.9%), whereas the relative errors produced by PBE and B3LYP are greater than 2.3% and 1.4%, respectively. The calculated  $1000\ln^{122/116}\beta$  values of cassiterite shown in Fig. S1 in the supplementary materials indicate that the results at the LDA/DZVP level match the NRIXS results in Polyakov et al. (2005) best. Indeed, many previous studies have shown that the structures and equilibrium isotope fractionation factors of minerals can be well predicted at the LDA level (e.g., Wentzcovitch et al., 2010; Wu and Wang, 2016; Qin et al., 2016; Zhang et al., 2018). Therefore, for megawite and romarchite, the calculations were performed at the LDA level with DZVP basis sets.

### 3. RESULTS

#### 3.1. $\text{Sn}^{2+}$ —Cl<sup>-</sup>/OH<sub>2</sub> complexes in aqueous solutions (below the critical point)

##### 3.1.1. Structures

The temporal fluctuations in Sn—Cl distances in the simulations of  $\text{SnCl}_4^{2-}$  in aqueous solutions are shown in Fig. 1. The stability of  $\text{SnCl}_4^{2-}$  can be reflected from these trajectories. Although  $\text{SnCl}_4^{2-}$  did not completely dissociate at 330 K in the simulation period, it could be seen in Fig. 1a there was always one Cl that was weakly attached to Sn with a long bond length (i.e., beyond the range of Sn—Cl distance of 3.0 Å). This implies a low stability of  $\text{SnCl}_4^{2-}$  even under ambient conditions. At 368 K, one Cl detached from Sn after 20.0 ps (the red line in Fig. 1b). At 573 K, the dissociation occurred more rapidly, i.e., within 5.0 ps (see Fig. S2 in the supplementary materials). These simulations indicate that  $\text{SnCl}_4^{2-}$  should only exist under ambient conditions, but is not stable in hydrothermal fluids.

The radial distribution functions (RDFs) and coordination numbers (CNs) curves for Cl and O around Sn for different aqueous Sn(II)—Cl species are shown in Fig. 2. At 330 K,  $\text{SnCl}_4^{2-}$  has a seesaw geometry (Fig. 2c) with Sn—Cl

RDF ranging from 2.32 Å to about 3.69 Å, and peaking at 2.62 Å (Fig. 2a). The corresponding CN curve amounts to an average coordination number of 3.2 at 3.0 Å. There is no obvious peak in Sn—O RDF (Fig. 2b), indicating that  $\text{Sn}^{2+}$  does not form any stable bond with water molecule.

$\text{SnCl}_3^-$  has a pyramidal geometry in aqueous solutions with an average Sn—Cl bond length of 2.58 Å at 330 K and 2.55 Å at 573 K, respectively (see the RDFs and snapshot in Fig. 2d and 2f). These distances are slightly longer than the previous EXAFS result (2.47 Å) (Sherman et al., 2000). No obvious peaks can be seen in the Sn—O RDFs of  $\text{SnCl}_3^-$  (Fig. 2e), indicating no Sn—OH<sub>2</sub> coordination.

For  $\text{SnCl}_2$  at 330 K and 573 K, the Sn—Cl RDF peaks are centered at 2.58 Å and 2.55 Å, respectively (Fig. 2g). The first Sn—O RDF peak occurs at 2.38 Å and 2.42 Å for 330 K and 573 K respectively, and their corresponding CN curves at 3.0 Å amount to about 2.1 and 1.6 at 330 K and 573 K respectively (Fig. 2h). The hydration structure of  $\text{SnCl}_2$  can be reflected based on Sn—OH<sub>2</sub> distance trajectories extracted from FPMD simulations in Fig. 3a. It can be seen that there is one water molecule coordinating with  $\text{Sn}^{2+}$  with a bond length of about 2.4 Å, and other water molecules interact with  $\text{SnCl}_2(\text{H}_2\text{O})$  at slightly greater distances. In the snapshot of Fig. 2i, the pyramidal geometry of  $\text{SnCl}_2(\text{H}_2\text{O})$  and a weakly bonded water molecule is shown. Such geometry of  $\text{SnCl}_2(\text{H}_2\text{O})$  persists at a higher temperature of 573 K (see the trajectories in Fig. S3a in the supplementary materials). The Sn—OH<sub>2</sub> distance trajectories show that the ligand exchange (i.e., between the coordinated and the solvent water molecules) is very frequent, i.e., at a timescale of 10.0 ps, implying that the Sn—OH<sub>2</sub> bonding cannot be strong.

Similar to the complexes above, the average Sn—Cl bond length in  $\text{SnCl}^+$  was not significantly influenced by temperature, i.e., 2.55 Å at 330 K and 2.49 Å at 573 K (Fig. 2j). As shown in the Sn—OH<sub>2</sub> distance trajectory plots at 330 K (Fig. 3b), one water ligand (the red line) of  $\text{SnCl}^+$  did not escape in the simulation period (i.e., 50.0 ps), while the other one (the black line) could exchange with the solvent water (i.e., from 25.0 ps to 30.0 ps in Fig. 3b). At 573 K, the water exchange happened more frequently (see

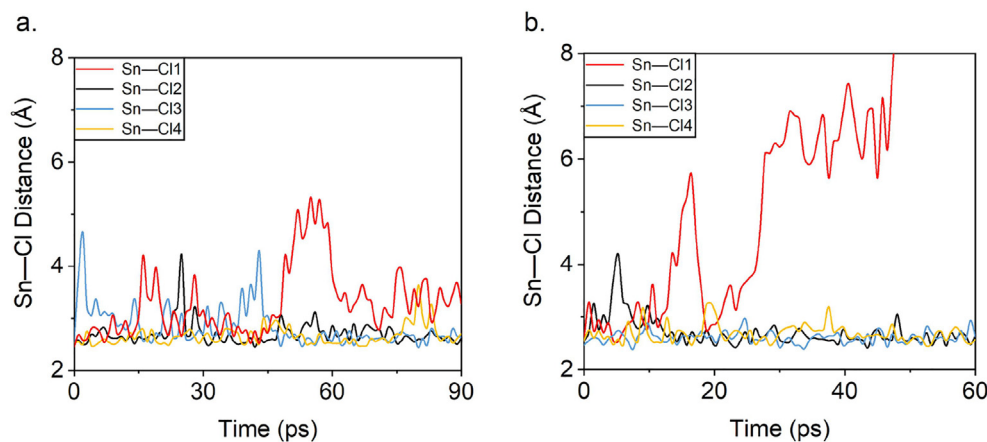


Fig. 1. Trajectories of Sn—Cl distances (annotated by different colors) in the simulations of  $\text{SnCl}_4^{2-}$  in aqueous solutions at (a) 330 K and (b) 368 K. Trajectories at 573 K are shown in Fig. S2 in the supplementary materials. At 330 K, there is always one Sn—Cl bond that is longer than the others and can reach up to 6.0 Å, which implies low stability. At higher temperatures (i.e., 368 K and 573 K), one Cl escaped spontaneously.

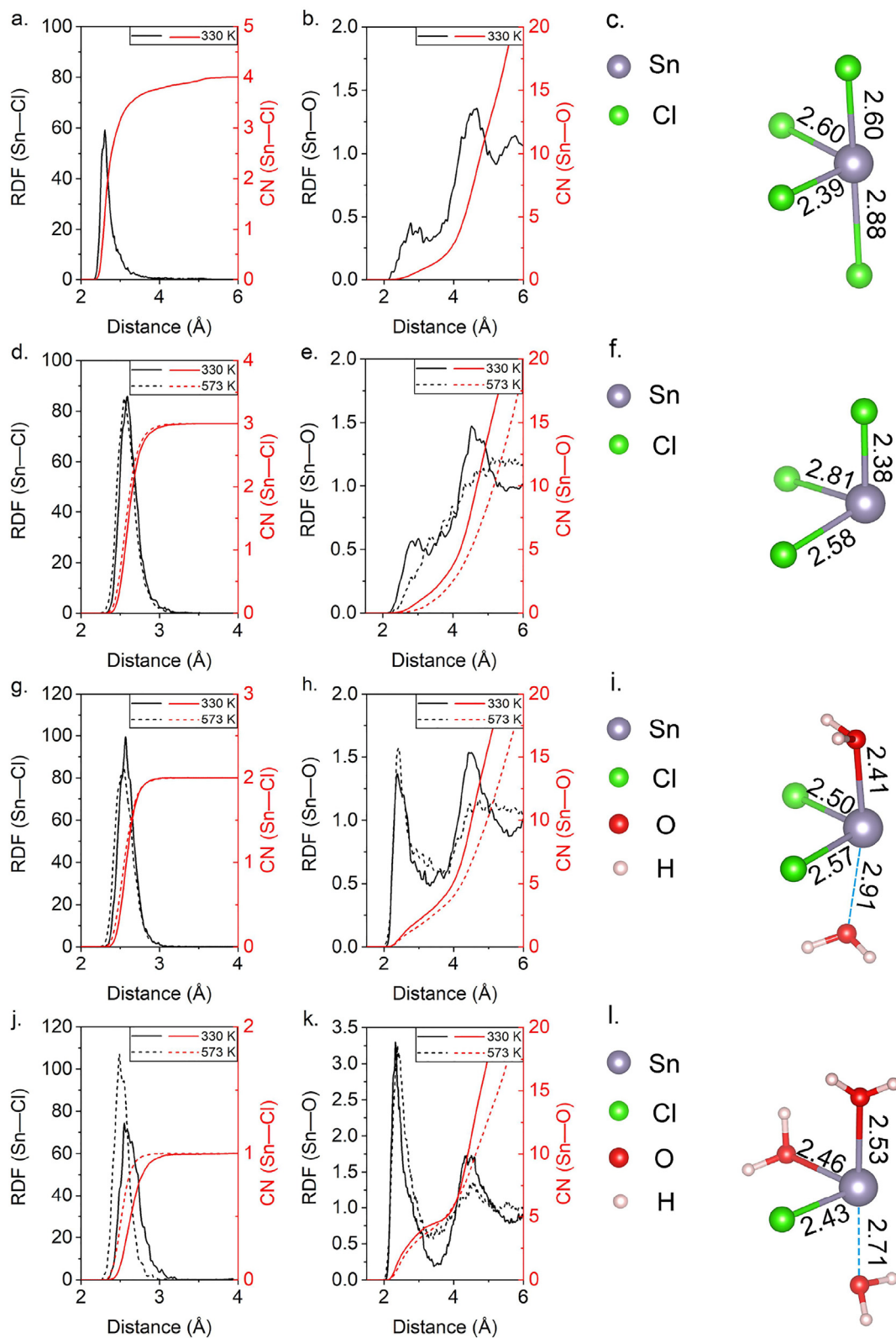


Fig. 2. RDF and CN curves for Cl and O around Sn and corresponding snapshots (at 330 K) in the simulations of (a–c)  $\text{SnCl}_4^{2-}$ , (d–f)  $\text{SnCl}_3^-$ , (g–i)  $\text{SnCl}_2$  and (j–l)  $\text{SnCl}^+$  in aqueous solutions. Blue dashed lines denote the weak Sn–OH<sub>2</sub> bonding in aqueous  $\text{SnCl}_2$  and  $\text{SnCl}^+$ . Bond lengths (in angstrom) are shown in the snapshots. Most of the solvent water molecules are removed for clarity.

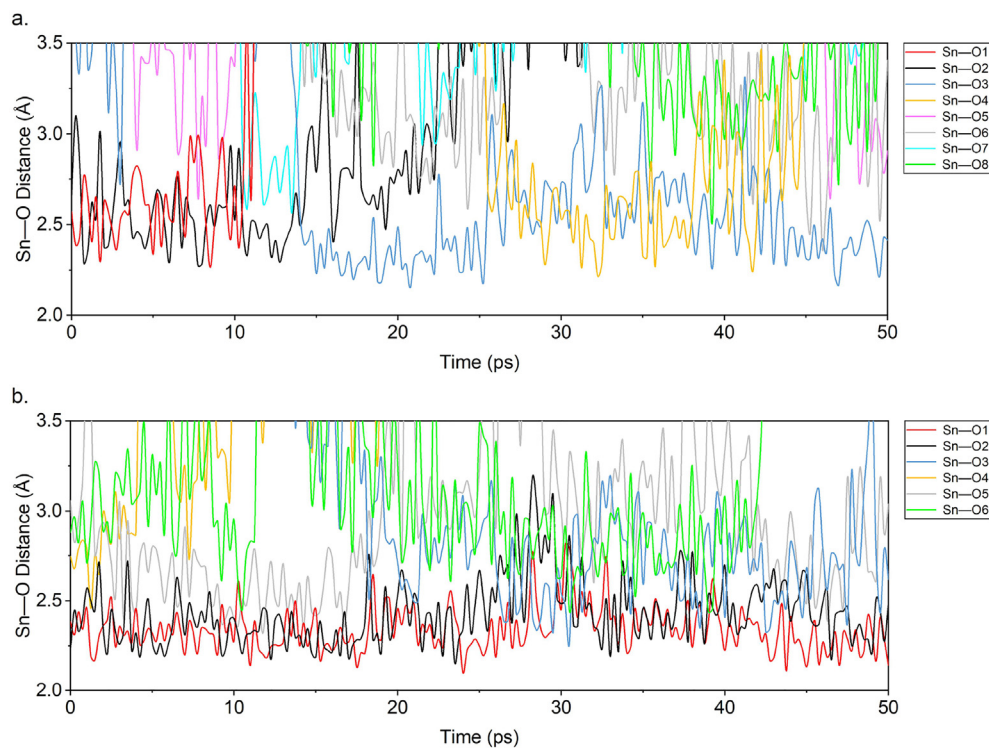


Fig. 3. Trajectories of Sn–OH<sub>2</sub> distances in the simulations of (a) SnCl<sub>2</sub> and (b) SnCl<sup>+</sup> in aqueous solutions at 330 K. Trajectories at 573 K are shown in Fig. S3 in the supplementary materials. For aqueous SnCl<sub>2</sub> and SnCl<sup>+</sup>, there are always one and two water molecules around Sn within 2.5 Å, respectively. Other water molecules can be found at slightly larger distances, i.e., in the range of 2.5 Å to 3.0 Å. The hydrations of SnCl<sub>2</sub> and SnCl<sup>+</sup> (i.e., SnCl<sub>2</sub>(H<sub>2</sub>O) and SnCl(H<sub>2</sub>O)<sub>2</sub><sup>+</sup>) can be reflected according to these trajectories.

the trajectories at 573 K in Fig. S3b in the supplementary materials). The average Sn–O bond lengths are 2.33 Å at 330 K and 2.40 Å at 573 K (Fig. 2k). According to the Sn–OH<sub>2</sub> distances trajectories, there are also some weak Sn–OH<sub>2</sub> bonding, which lead to the Sn–O CNs at 3.0 Å amounting to about 3.7 at 330 K and 3.2 at 573 K (Fig. 2k). These simulations show that the aqueous complex should be SnCl(H<sub>2</sub>O)<sub>2</sub><sup>+</sup> (see the snapshot in Fig. 2l).

For the hydration structure of Sn<sup>2+</sup> at ambient conditions, the RDF curve derived from FPMD simulation shows an average Sn–O bond length of 2.31 Å. The first RDF peak ends at 3.4 Å and the corresponding CN amounts to about 5.4 (see the RDF and CN curves in Fig. 4a). The Sn–OH<sub>2</sub> distance trajectories plotted in Fig. S4a in the supplementary materials show a three-fold coordination. This result is consistent with the X-ray absorption spectroscopy (XAS) and X-ray scattering results (Persson et al., 2016; Yamaguchi et al., 1982; Johansson and Ohtaki, 1973). At 573 K, the average Sn–O bond length is also 2.31 Å, and the corresponding CN curve amounts to about 5.3 at 3.3 Å, where the first RDF peak ends. In the Sn–OH<sub>2</sub> distance trajectories plotted in Fig. S4b in the supplementary materials, it can be seen that Sn<sup>2+</sup> is also three-coordinated at 573 K.

### 3.1.2. Stability

In this section, we focus on the stability of SnCl<sub>4</sub><sup>2-</sup>, SnCl<sub>3</sub><sup>-</sup>, SnCl<sub>2</sub> and SnCl<sup>+</sup> in aqueous solutions, and the free energy profiles for their dissociation reactions are

shown in Fig. 5. Since the Sn–Cl distance trajectories in Fig. 1b has shown that SnCl<sub>4</sub><sup>2-</sup> is unstable at elevated temperatures, i.e., 368 K and 573 K, we only calculated the free energy change for its dissociation at ambient conditions. The free energy change of SnCl<sub>4</sub><sup>2-</sup> dissociation at ambient conditions is only 0.6 ± 0.5 kcal/mol, which confirms the low stability of SnCl<sub>4</sub><sup>2-</sup>. At 4.6 Å, the dissociating Cl<sup>-</sup> was separated from Sn<sup>2+</sup> by a water molecule (Fig. 5a), and thus it was taken as the end of the dissociation process.

The free energy changes from SnCl<sub>3</sub><sup>-</sup> to SnCl<sub>2</sub>(H<sub>2</sub>O) are 4.1 ± 0.6 kcal/mol and 7.5 ± 0.8 kcal/mol at 330 K and 573 K, respectively. Here we take the dissociation process at 330 K as an example as that is similar at 573 K. As shown in Fig. 5b, the free energy increased as one Cl<sup>-</sup> was drawn away from Sn<sup>2+</sup>. After reaching a maximum at a Sn–Cl distance of 4.0 Å, the free energy curve in Fig. 5b bent downwards slightly, and reached a minimum at 4.6 Å. At this point, Cl<sup>-</sup> and Sn<sup>2+</sup> was separated by water molecules, marking the end of the dissociation process.

The free energy changes for SnCl<sub>2</sub>(H<sub>2</sub>O) dissociation are 6.5 ± 0.6 kcal/mol and 7.9 ± 0.7 kcal/mol at 330 K and 573 K, respectively. The structures of aqueous SnCl<sub>2</sub>(H<sub>2</sub>O) derived from the FPMD simulations at 330 K and 573 K (as shown in Fig. 2i) were taken as the initial configurations. At 330 K, the free energy firstly increased and reached the maximum value at 4.0 Å. After that a minimum occurred at 5.0 Å. As shown in in Fig. 5c, at this point a

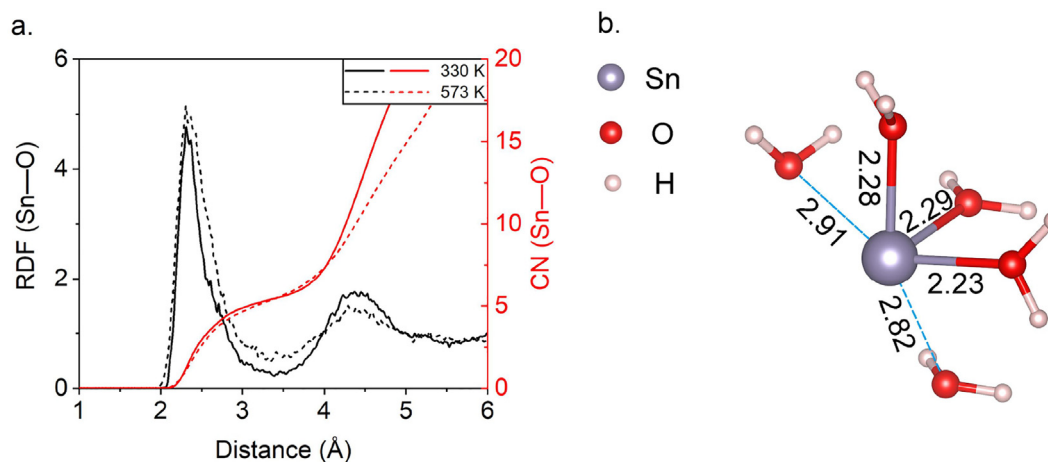


Fig. 4. (a) RDF and CN curves for O around Sn and (b) snapshot of hydrated  $\text{Sn}^{2+}$  at 330 K. Blue dashed lines denote the weak Sn—OH<sub>2</sub> bonding. Bond lengths (in angstrom) are shown in the snapshots. Most of the solvent water molecules are removed for clarity.

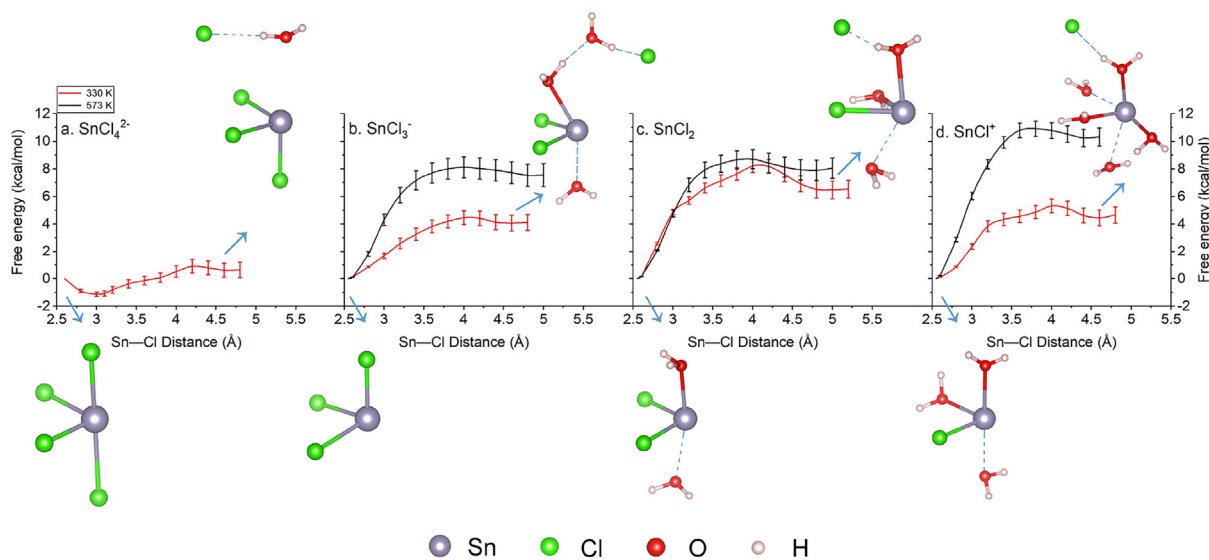


Fig. 5. Free energy profiles of dissociation for (a)  $\text{SnCl}_4^{2-}$  (b)  $\text{SnCl}_3^-$  (c)  $\text{SnCl}_2$  and (d)  $\text{SnCl}^+$  in aqueous solutions. Snapshots of the initial and final configurations at 330 K are shown. Blue dashed lines represent the weak bonding. Most of the solvent water molecules are removed for clarity.

water molecule separated the dissociating  $\text{Cl}^-$  from  $\text{Sn}^{2+}$ , pinpointing the end of  $\text{SnCl}_2(\text{H}_2\text{O})$  dissociation.

The free energy changes for  $\text{SnCl}(\text{H}_2\text{O})_2^+$  dissociation are  $4.4 \pm 0.6$  kcal/mol and  $10.2 \pm 0.6$  kcal/mol at 330 K and 573 K, respectively. At ambient conditions, the maximum value of the free energy curves occurred at 4.0 Å and the minimum occurred at 4.6 Å, respectively. Similar to the dissociation processes of  $\text{SnCl}_3^-$  and  $\text{SnCl}_2(\text{H}_2\text{O})$ , one solvent water molecules became coordinated with  $\text{Sn}^{2+}$  as  $\text{Cl}^-$  moved away from  $\text{Sn}^{2+}$ , forming  $\text{Sn}(\text{H}_2\text{O})_3^{2+}$  at last (Fig. 5d).

According to the above results, free energy changes for the dissociation of  $\text{SnCl}_3^-$ ,  $\text{SnCl}_2(\text{H}_2\text{O})$  and  $\text{SnCl}(\text{H}_2\text{O})_2^+$  at 573 K are larger than those at ambient conditions. The free energy data indicate that  $\text{SnCl}_3^-$  is the more stable Sn (II)—Cl species in hydrothermal solutions up to 573 K.

### 3.2. $\text{Sn}^{2+}$ —Cl<sup>-</sup> complexes in supercritical aqueous fluids

Supercritical water has low dielectric constant (e.g., 12.06 at 773 K–1.5 kbar and 4.83 at 973 K–1.5 kbar according to Sverjensky et al. (2014)), and therefore neutral species such as  $\text{SnCl}_2$  are favored under these conditions. FPMD simulations indicated that  $\text{SnCl}_2$  was stable at 773 K–1.5 kbar and 973 K–1.5 kbar, with average Sn—Cl bond lengths of 2.50 Å and 2.45 Å, respectively (Fig. 6a). The average Cl—Sn—Cl angles are 97.3° and 99.6° at 773 K–1.5 kbar and 973 K–1.5 kbar, respectively. The average Sn—Cl bond length is shorter than that in hydrothermal solutions below the critical point (i.e., 2.58 Å at 330 K and 2.55 Å at 573 K), which can be attributed to the very weak Sn—OH<sub>2</sub> bonding under supercritical conditions (i.e., water molecules can coordinate with  $\text{Sn}^{2+}$  sporadically; see the

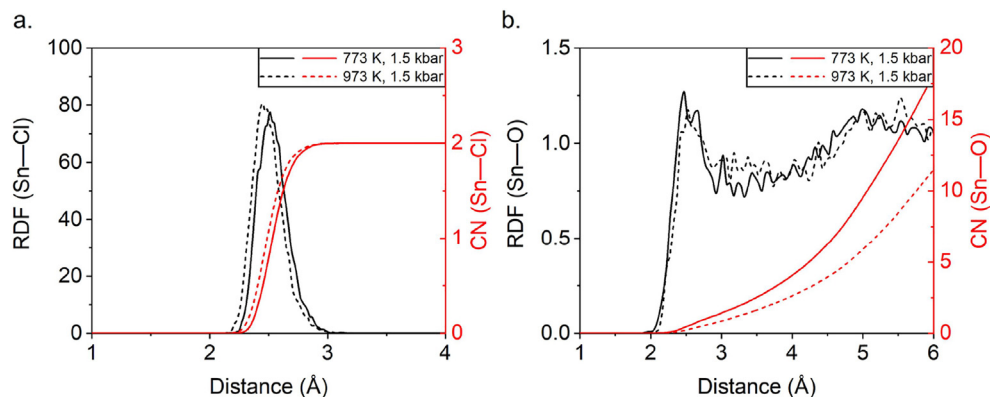


Fig. 6. RDF and CN curves for (a) Cl and (b) O around Sn in the simulations of  $\text{SnCl}_2$  in supercritical aqueous fluids.

$\text{Sn-O}$  RDF and CN curves in Fig. 6b). The static calculations for gaseous  $\text{SnCl}_2$  and  $\text{SnCl}_2(\text{H}_2\text{O})$  (see Section 3.3) also indicated that  $\text{Sn-OH}_2$  bonding leads to longer  $\text{Sn-Cl}$  bond length and that the  $\text{Sn-Cl}$  bond lengths in gaseous  $\text{SnCl}_2$  and  $\text{SnCl}_2(\text{H}_2\text{O})$  are 2.39 Å and 2.44 Å, respectively. The  $\text{Cl-Sn-Cl}$  angles in gaseous  $\text{SnCl}_2$  and  $\text{SnCl}_2(\text{H}_2\text{O})$  are 99.6° and 99.5° respectively, close to the average  $\text{Cl-Sn-Cl}$  angle in supercritical aqueous fluids.

### 3.3. Sn(II) species in vapor phases

$\text{SnCl}_2$  is the dominant Sn(II) species in vapor phases (see below). The calculated  $\text{Sn-Cl/O}$  bond lengths,  $\text{Cl-Sn-Cl}$  angle, and vibrational frequencies of gaseous  $\text{SnCl}_2$  and  $\text{SnO}$  molecules are listed in Table 2. Computational and experimental results in previous studies are tabulated for comparison.  $\text{SnCl}_2$  has a trigonal geometry with the  $\text{Sn-Cl}$  bond lengths of 2.390 Å and the  $\text{Cl-Sn-Cl}$  angle of 99.6° at the B3LYP/def2-TZVP level. At the CCSD(T)/aug-cc-pVTZ(-pp) and the CCSD(T)/aug-cc-pVQZ(-pp) level, the  $\text{Sn-Cl}$  bond lengths in  $\text{SnCl}_2$  are 2.371 Å and 2.352 Å respectively, and the  $\text{Cl-Sn-Cl}$  angles are 97.8° and 97.6° respectively. The  $\text{Sn-O}$  bond length in gaseous  $\text{SnO}$  at the B3LYP/def2-TZVP level is 1.832 Å. These parameters are consistent with the results of previous *ab initio* studies as summarized in Table 2, and the differences between calculated vibrational frequencies at the B3LYP/def2-TZVP level and experimental results are within 5.4%. These comparisons confirm that the Sn(II)-Cl and Sn(II)-O interactions can be reasonably reproduced by the DFT level applied. The optimized structures of other gaseous Sn(II) species are shown in Fig. S5 in the supplementary materials.

In addition, the optimized structures of  $\text{SnCl}_3^-$  and  $\text{SnCl}_2(\text{H}_2\text{O})$  with 18 solvent water molecules are also shown in Fig. S6. The  $\text{Sn-Cl}$  bond lengths in the optimized structures of aqueous  $\text{SnCl}_3^-$  (Fig. S6a) are 2.55 Å, 2.58 Å and 2.67 Å, respectively, which are within the ranges of  $\text{Sn-Cl}$  RDF peaks (2.3–3.5 Å; Fig. 2d). The shortest  $\text{Sn-OH}_2$  distance is 2.82 Å, indicating a weak  $\text{Sn-OH}_2$  bonding as shown in  $\text{Sn-O}$  RDF in Fig. 2f. In the optimized structures of aqueous  $\text{SnCl}_2(\text{H}_2\text{O})$ , the  $\text{Sn-Cl}$  bond lengths are 2.54 Å and 2.83 Å, respectively (Fig. S6b), consistent with the

ranges of  $\text{Sn-Cl}$  RDF peaks (2.3–3.1 Å; Fig. 2g). The  $\text{Sn-OH}_2$  distances within 3.0 Å are 2.21 Å and 2.54 Å respectively, consistent with the FPMD geometry of  $\text{SnCl}_2(\text{H}_2\text{O})$  having a weakly bonded water molecule in aqueous solutions. These comparisons indicate that the optimized structures of aqueous species can represent the structures derived from FPMD simulations reasonably.

The Gibbs free energy changes ( $\Delta G$ ) of the reactions among possible gaseous Sn(II) species from ambient to elevated conditions were calculated at the B3LYP/def2-TZVP level and listed in Table 3. The  $\Delta G$  value for the reaction of  $\text{SnO}$  to  $\text{SnCl}_2$  is negative, e.g., -60.44 kcal/mol at ambient conditions and -60.32 kcal/mol at 573 K. The  $\Delta G$  values for the reaction of  $\text{SnCl}_2(\text{HCl})/\text{SnCl}(\text{OH})/\text{Sn}(\text{OH})_2$  are also negative. These results indicate that  $\text{SnCl}_2$  is more stable than  $\text{SnO}/\text{SnCl}_2(\text{HCl})/\text{SnCl}(\text{OH})/\text{Sn}(\text{OH})_2$ . It should be noted that the  $\Delta G$  values for the dehydration reaction of  $\text{SnCl}_2(\text{H}_2\text{O})$  are quite small, indicating similar stability of  $\text{SnCl}_2(\text{H}_2\text{O})$  and  $\text{SnCl}_2$  in vapors.

### 3.4. Equilibrium Sn isotope fractionation factors

The calculated  $1000\ln^{122/116}\beta$  values of Sn(II)-Cl species (at the B3LYP/def2-TZVP level) and Sn-bearing minerals (at the LDA/DZVP level) as a function of temperature are tabulated in Table 4, and shown in Figs. 7 and 8. The computational results of Sn(IV) chloride species by She et al. (2020) and the NRXS results of Sn-bearing minerals in Polyakov et al. (2005) are also plotted in Figs. 7 and 8 for comparison. Comparison between the optimized lattice parameters and calculated  $1000\ln^{122/116}\beta$  values of  $2 \times 2 \times 4$  and  $3 \times 3 \times 5$  cassiterite supercells, as well as  $2 \times 2 \times 2$  and  $3 \times 3 \times 3$  megawite supercells, is tabulated in Tables S1 and S2 in the supplementary materials. The calculated  $1000\ln^{122/116}\beta$  values at other levels, i.e., values for  $\text{SnCl}_2$  and  $\text{SnCl}_4$  at the CCSD(T)/aug-cc-pVTZ(-pp) level and values for  $\text{SnCl}_4$ , *cis*- $\text{SnCl}_4(\text{H}_2\text{O})_2(\text{aq})$ ,  $\text{SnCl}_3^-(\text{aq})$ , cassiterite at the B3LYP/TZVP level, together with the relevant vibrational frequencies data, are tabulated in the supplementary materials.

For Sn(II)-Cl species, there is no obvious difference in  $1000\ln^{122/116}\beta$  values of aqueous species between the 18

Table 4  
Calculated  $1000\ln^{122/116}\beta$  values for aqueous and gaseous Sn chlorides and Sn-bearing minerals.<sup>a</sup>

System	25 °C	96 °C	300 °C	500 °C	700 °C
<i>Sn(II) chlorides</i>					
SnCl <sub>2</sub>	2.62	1.73	0.73	0.40	0.25
SnCl <sub>2</sub> (H <sub>2</sub> O)	2.77	1.83	0.77	0.43	0.27
SnCl <sub>3</sub> <sup>-</sup> + 18 H <sub>2</sub> O	2.18	1.43	0.60	0.33	0.21
SnCl <sub>2</sub> (H <sub>2</sub> O) + 18 H <sub>2</sub> O	2.45	1.62	0.68	0.38	0.24
<i>Sn(IV) chlorides<sup>b</sup></i>					
SnCl <sub>4</sub>	6.56	4.35	1.84	1.02	0.64
SnCl <sub>6</sub> <sup>2-</sup> + 18 H <sub>2</sub> O	4.72	3.11	1.30	0.72	0.45
<i>cis</i> -SnCl <sub>4</sub> (H <sub>2</sub> O) <sub>2</sub> + 18 H <sub>2</sub> O	6.03	4.00	1.70	0.94	0.60
<i>Minerals</i>					
Cassiterite (SnO <sub>2</sub> ) <sup>c</sup>	7.85	5.21	2.21	1.22	0.77
Megawite (CaSnO <sub>3</sub> ) <sup>d</sup>	7.71	5.11	2.16	1.19	0.76
Romarchite (SnO)	3.13	2.05	0.86	0.47	0.30

<sup>a</sup> Data for aqueous and gaseous species were calculated at the B3LYP/def2-TZVP level. Data for minerals were calculated at the LDA/DZVP level.

<sup>b</sup> Data from She et al. (2020), calculated at the B3LYP/def2-TZVP level.

<sup>c</sup> Calculated using the 2 × 2 × 4 supercell.

<sup>d</sup> Calculated using the 2 × 2 × 2 supercell.

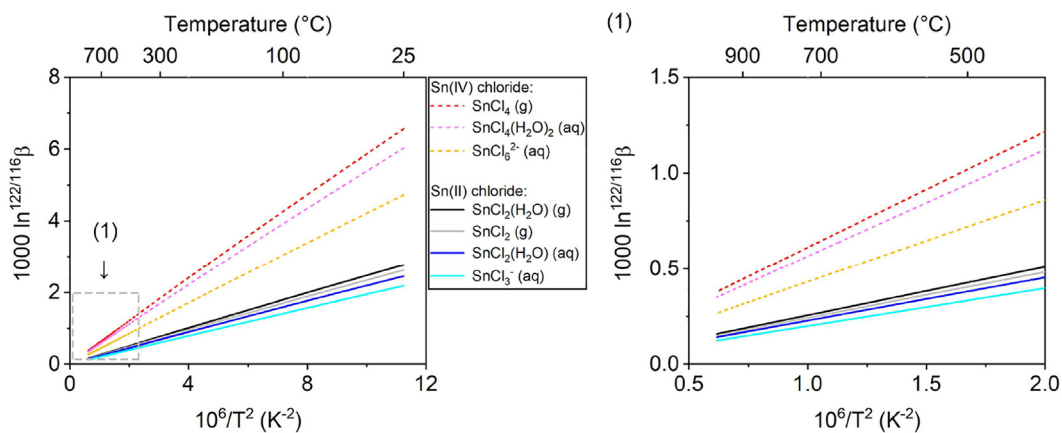


Fig. 7. Calculated  $1000\ln^{122/116}\beta$  values for Sn chlorides in aqueous solutions and vapor phases (at the B3LYP/def2-TZVP level).

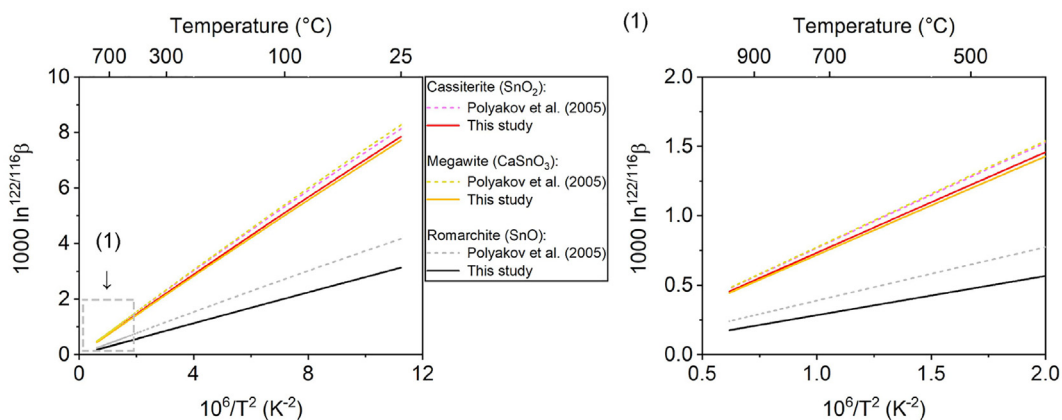


Fig. 8. Calculated  $1000\ln^{122/116}\beta$  values for Sn-bearing minerals (at the LDA/DZVP level).

and 24 solvent water molecules for Sn(II) chlorides (see Table S4 in the supplementary materials), as has been demonstrated for aqueous Sn(IV) chlorides (She et al., 2020). Therefore, we only show the results of the models with 18 solvent water molecules in Table 4 and Fig. 7. As shown in Fig. 7, the enrichment of  $^{122}\text{Sn}$  decreases in the order  $\text{SnCl}_4(\text{g}) > \text{cis-}/\text{trans-SnCl}_4(\text{H}_2\text{O})_2(\text{aq}) > \text{SnCl}_6^{2-}(\text{aq}) > \text{SnCl}_2(\text{H}_2\text{O})(\text{g}) > \text{SnCl}_2(\text{g}) > \text{SnCl}_2(\text{H}_2\text{O})(\text{aq}) > \text{SnCl}_3^- (\text{aq})$ . The equilibrium Sn isotope fractionations among Sn (II) chlorides are much smaller than the values among Sn (IV) chlorides. From ambient temperature to 1000 °C, the  $1000\ln^{122/116}\beta$  values for  $\text{SnCl}_4$  and  $\text{SnCl}_2$  calculated from the DFT level applied are slightly (i.e., within  $-10.5\%$  of relative error) smaller than those calculated from the CCSD(T) level. For instance, at 25 °C, the  $1000\ln^{122/116}\beta$  values for  $\text{SnCl}_4$  and  $\text{SnCl}_2$  calculated at the CCSD(T)/aug-cc-pVTZ(-pp) level are 7.28 ‰ and 2.91 ‰, respectively, and the corresponding values at the B3LYP/def2-TZVP level are 6.56 ‰ and 2.62 ‰, respectively.

The optimized lattice parameters of the minerals are listed in Table S1 in the supplementary materials. The calculated lattice parameters at the LDA/DZVP level match with the experiments within 1.1% except that the c-axis length of romarchite cell is underestimated by 3.0%. This discrepancy is due to the inability of semilocal functionals in accounting for the interlayer van der Waals interactions (Perdew and Ruzsinszky, 2010; Grimme, 2011; Méheut and Schauble, 2014). There is no significant difference between the optimized lattice parameters and calculated  $1000\ln^{122/116}\beta$  values of cassiterite and megawite with different size of supercells (see Tables S1 and S2 in the supplementary materials), indicating that a  $2 \times 2 \times 4$  supercell for cassiterite and a  $2 \times 2 \times 2$  supercell for megawite are sufficient. The calculated  $1000\ln^{122/116}\beta$  values for cassiterite calculated with different functionals (i.e., LDA, PBE and B3LYP) and basis sets (i.e., DZVP and TZVP) shown in Fig. S1 in the supplementary materials indicate that the results at the LDA/DZVP level match the NRIXS results in Polyakov et al. (2005) well (with relative errors within  $-4.6\%$ ). As shown in Table 4 and Fig. 8, the calculated  $1000\ln^{122/116}\beta$  values of megawite at the LDA/DZVP level are also very close to the NRIXS results, and there is no significant equilibrium Sn isotope fractionation between cassiterite and megawite. The difference in  $1000\ln^{122/116}\beta$  values for romarchite between the results in this study and Polyakov et al. (2005) is slightly greater (i.e., 1.04 ‰ at 25 °C).

## 4. DISCUSSION

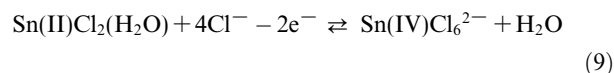
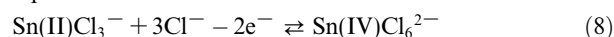
### 4.1. Sn chloride complexation in hydrothermal fluids

The results show that the stable Sn(II)—Cl species include  $\text{SnCl}_3^-$ ,  $\text{SnCl}_2(\text{H}_2\text{O})$  and  $\text{SnCl}(\text{H}_2\text{O})_2^+$  in aqueous solutions (below the critical point),  $\text{SnCl}_2$  and  $\text{SnCl}_2(\text{H}_2\text{O})$  in vapor, and  $\text{SnCl}_2$  in supercritical fluids. Free energy calculations indicate that  $\text{SnCl}_3^-$  is the dominant Sn(II)—Cl complex from ambient conditions to 300 °C in aqueous solutions.  $\text{SnCl}_4^{2-}$  can only exist with very low stability at ambient conditions, and is not important at elevated tem-

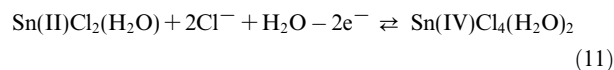
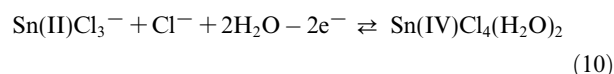
peratures. These results are consistent with the *in situ* UV spectroscopy study on hydrothermal Sn(II)—Cl species by Müller and Seward (2001), who suggested that  $\text{SnCl}_3^-$  and  $\text{SnCl}_2$  are the dominant species up to 300 °C and  $\text{SnCl}_4^{2-}$  is stable only at low temperatures. In supercritical aqueous fluids,  $\text{SnCl}_2$  is stable, which is consistent with the previous solubility experiments (Wilson and Eugster, 1990; Taylor and Wall, 1993; Duc-Tin et al., 2007). During evaporation of Sn(IV) chloride solution in air,  $\text{SnCl}_4$  is the dominant gaseous Sn(IV) species (She et al., 2020). By contrast, calculations in this study show that Sn can be transported in vapor phases in the form of  $\text{SnCl}_2$  and  $\text{SnCl}_2(\text{H}_2\text{O})$  under reduced conditions.

Results in this study, together with previous studies of Sn(IV) chloride species (Sherman et al., 2000; Schmidt, 2018; She et al., 2020), place strong constraints on the speciation of Sn(II/IV)—Cl complexes in hydrothermal fluids, and provide a physical basis for understanding the transport and mineralization of Sn. Although the dominance of Sn(IV) chloride species in aqueous solutions remains a controversial topic, e.g.,  $\text{SnCl}_6^{2-}$  in Sherman et al. (2000) vs.  $\text{SnCl}_4(\text{H}_2\text{O})_2$  (Schmidt, 2018), FPMD simulations have indicated that both of them are stable at ambient conditions and 95 °C (She et al., 2020). Additionally, the detailed geometries of Sn—Cl species derived from the first principles calculations indicate that the Sn—Cl/O bonds in Sn (II) species are longer than that in Sn(IV) species. For example, the average Sn—Cl bond lengths in  $\text{Sn}(\text{II})\text{Cl}_3^-$ ,  $\text{Sn}(\text{II})\text{Cl}_2(\text{H}_2\text{O})$ ,  $\text{Sn}(\text{IV})\text{Cl}_6^{2-}$  and  $\text{Sn}(\text{IV})\text{Cl}_4(\text{H}_2\text{O})_2$  in aqueous solutions at ambient conditions are 2.58 Å, 2.58 Å, 2.48 Å and 2.45 Å, respectively.

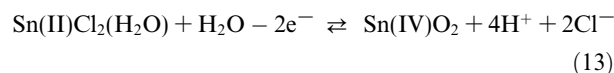
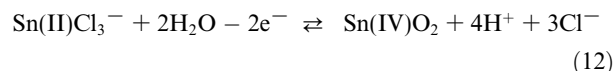
Compared with  $\text{Sn}^{2+}$ ,  $\text{Sn}^{4+}$  coordinates with more  $\text{Cl}^-$  in hydrothermal fluids. The transformation between  $\text{SnCl}_3^-/\text{SnCl}_2(\text{H}_2\text{O})$  and possible Sn(IV)—Cl complexes can be expressed as:



or



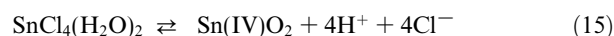
and the precipitation of cassiterite from hydrothermal fluids can be expressed as:



with



or



Eqs. (8)–(11) imply that during the transport of Sn in geological fluids, higher  $\text{Cl}^-$  activity can enhance the conversion to Sn(IV)–Cl complexes, which can facilitate the formation of tin deposits as tin exists as tetravalence in cassiterite. This is supported by fluid inclusion studies on Sn deposits. For example, Müller et al. (2001) reported high salinity (up to 22 wt% NaCl equiv.) in Sn-mineralizing fluids from the Huanuni tin deposit, Bolivia. A statistical study in Naumov et al. (2011) show that more than 25 wt % of fluid inclusions from tin deposits have salinity >20 wt% NaCl equiv. On the other hand, Eqs. (12)–(15) show that cassiterite precipitation reactions are  $\text{H}^+$ -releasing processes, and therefore neutral to alkaline ( $\text{H}^+$ -consuming) environments can promote cassiterite mineralization. This is corroborated by the facts that hydrothermal Sn mineralization is generally associated with the alteration reactions of feldspars (greisenization) or carbonates (skarnization) (Heinrich, 1990; Lehmann, 1990; Chen et al., 2000). Additionally, the electron transfer in the oxidation of Sn(II)–Cl complexes in hydrothermal fluids, i.e., Eqs. (8)–(13), can be caused by the reduction of  $\text{Fe}^{3+}$ , which can be supported by the coexistence of cassiterite and some  $\text{Fe}^{2+}$ -bearing minerals such as pyrite or chalcopyrite in some tin deposits (e.g., Heinrich and Eadington, 1986; Schwartz et al., 1995; Pavlova et al., 2015). The dissolved oxygen can also oxidize  $\text{Sn}^{2+}$  because of the low redox potential for  $\text{Sn}^{4+}/\text{Sn}^{2+}$  in aqueous solutions (i.e.,  $E^\ominus(\text{Sn}^{4+}/\text{Sn}^{2+}) = 0.384 \pm 0.020$  V according to Gajda et al. (2009)).

#### 4.2. Sn isotope fractionation in ore-forming processes

A comparison of the  $\beta$  factors for the aqueous and gaseous Sn(II)–Cl and Sn(IV)–Cl species (Fig. 7) highlights the effects of redox potential and evaporation on the equilibrium Sn isotope fractionation. In geological fluids, heavy isotopes of metals preferentially partition into high valence species. For example, first principles calculations by Li and Liu (2011) and Wu et al. (2015a) indicated that high valence Se and V species enrich heavy isotopes. For both Sn(II)–Cl and Sn(IV)–Cl species, heavy Sn isotopes preferentially partition into the vapor phases relative to aqueous solutions. During hydrothermal mineralization processes, Sn is transported in hydrothermal fluids as vapor or aqueous species, then ultimately precipitated as Sn-bearing minerals. Cassiterite, the most important ore mineral for Sn, can precipitate via hydrolysis of Sn complexes in hydrothermal fluids. Figs. 7 and 8 shows that, regardless of the method to derive equilibrium Sn isotope fractionation data for cassiterite (i.e., the first principles calculation in this study or the NRIXS in Polyakov et al. (2005)), the obtained  $1000\ln^{122/116}\beta$  values of cassiterite are higher than those of all aqueous and gaseous Sn(II/IV)–Cl species. In other words, hydrothermal precipitation of cassiterite would be accompanied with preferential removal of heavy Sn isotopes from fluids under isotopic equilibrium.

Presently, a significant amount of Sn isotope data from natural cassiterite are available in literature (Yao et al., 2018; Wang et al., 2019a; Mason et al., 2020), from which a variability of 1.84‰ in  $\delta^{122/116}\text{Sn}$  has been reported (Fig. 9c). Although the Sn isotope data were measured from

separate mineral deposits without specific paragenetic and temperature constraints, the statistical properties (i.e., range and distribution pattern) of the  $\delta^{122/116}\text{Sn}$  values for cassiterite still hold invaluable clues for a deeper understanding Sn mineralization, with the help of a probabilistic model-driven approach that connects Sn isotopic variability of cassiterite to speciation of Sn in hydrothermal fluids. The core idea is to calculate a series of distribution pattern of  $\delta^{122/116}\text{Sn}$  values for hydrothermal cassiterite by assuming different Sn species in the hydrothermal system, then compare the derived distribution patterns of  $\delta^{122/116}\text{Sn}$  with the observed pattern of  $\delta^{122/116}\text{Sn}$  for natural cassiterite, and the best match would be indicative of the most important Sn speciation during cassiterite mineralization.

We firstly model the evolution of Sn isotope composition of hydrothermal fluids in a mineralization system following a transport-precipitation model of Li et al. (2010). In this model, we envision a high-Sn hydrothermal fluid of magmatic origin to exsolve from a fertile source pluton. As the fluid is transported away from the magma, its temperature decreases and cassiterite is precipitated due to the strong temperature dependence of cassiterite solubility in hydrothermal fluids (Audétat et al., 1998). Consequently, cassiterite of different stage would be precipitated along the fluid pathway. Sn in such theoretical scenario follows both elemental and isotopic mass balance:

$$F(n) = F(n+1) + C(n+1) \quad (16)$$

$$\delta^{122/116}\text{Sn}_{\text{fluid}}(n) \times F(n) = \delta^{122/116}\text{Sn}_{\text{fluid}}(n+1) \times F(n+1) + \delta^{122/116}\text{Sn}_{\text{cassiterite}}(n+1) \times C(n+1) \quad (17)$$

where  $\delta^{122/116}\text{Sn}_{\text{fluid}}$  denotes  $\delta^{122/116}\text{Sn}$  value of Sn in the hydrothermal fluid that contains a Sn mass of  $F(n)$  at a given stage ( $n$ ), and temperature drops and this fluid evolved to the next stage ( $n+1$ ), cassiterite is separated from the fluid, removing Sn that has a mass of  $C(n+1)$  and a Sn isotope composition of  $\delta^{122/116}\text{Sn}_{\text{cassiterite}}(n+1)$ , as a consequence, the Sn isotope composition of the fluid evolves to  $\delta^{122/116}\text{Sn}_{\text{fluid}}(n+1)$ , and the mass decreases to  $F(n+1)$ . The Sn isotope fractionation between the hydrothermal fluid and the precipitated cassiterite can be described as:

$$\Delta^{122/116}\text{Sn}_{\text{cassiterite-fluid}} = \delta^{122/116}\text{Sn}_{\text{cassiterite}}(n+1) - \delta^{122/116}\text{Sn}_{\text{fluid}}(n+1) \quad (18)$$

$\Delta^{122/116}\text{Sn}_{\text{cassiterite-fluid}}$  can be calculated based on the  $\beta$  factors (i.e.,  $\Delta\text{Sn}_{\text{A-B}} = 1000\ln\beta_{\text{A}} - 1000\ln\beta_{\text{B}}$ ) in this study and She et al. (2020), by assuming the dominance of a certain Sn species in the hydrothermal fluid (Fig. 9b). In this study, the results of aqueous and gaseous species calculated at the B3LYP/def2-TZVP level and the results of cassiterite calculated at the LDA/DZVP level were employed in the model (denoted as “Model-I”). To evaluate the potential influence of theoretical calculation level on the modeling results, we additionally tested another two other series of  $\beta$  factors as the input parameters of the transport-precipitation model: (1) the  $1000\ln^{122/116}\beta$  values for  $\text{SnCl}_4$  and  $\text{SnCl}_2$  at the CCSD(T)/aug-cc-pVTZ-(pp) level and the NRIXS results for cassiterite taken from Polyakov et al.

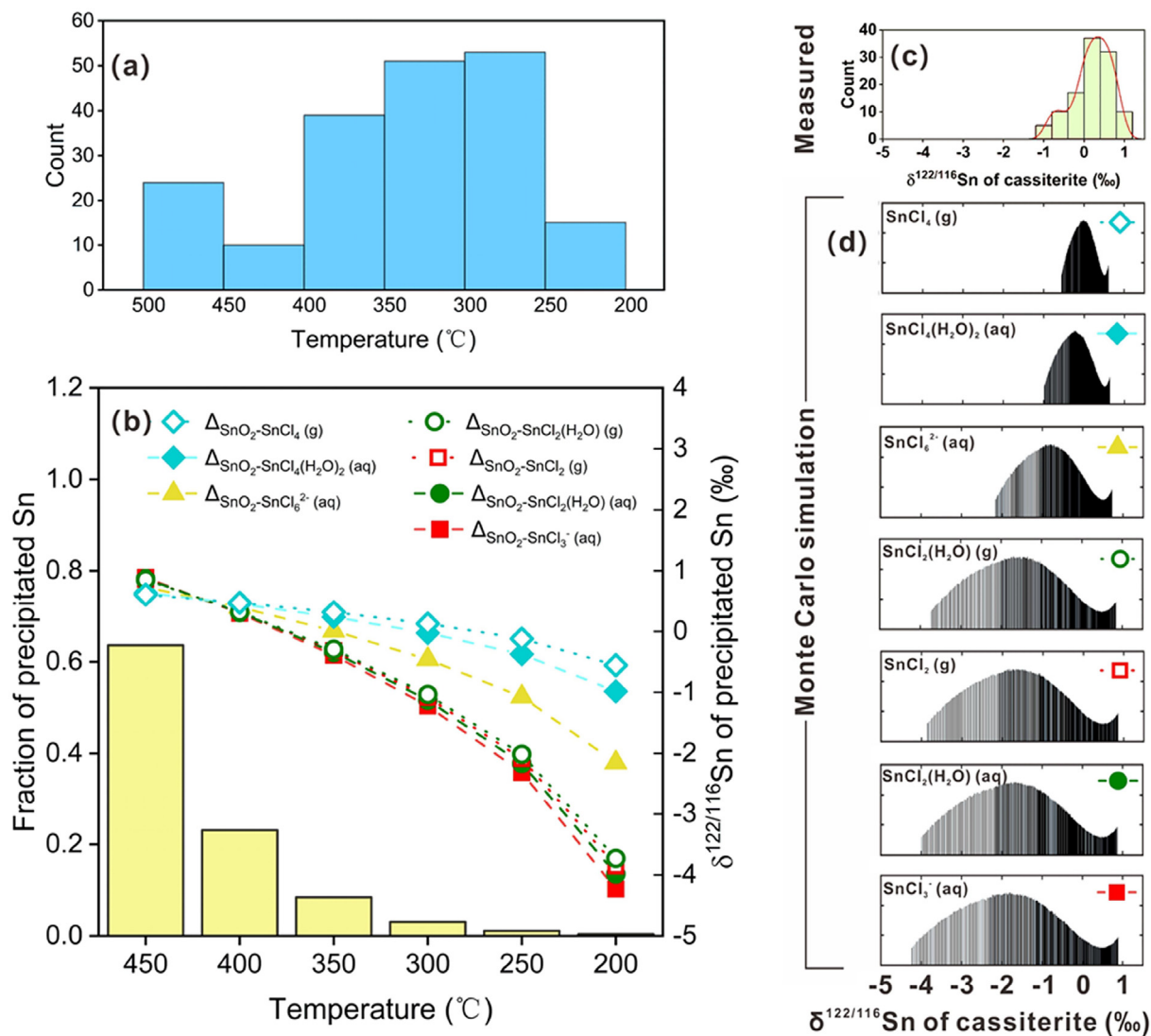


Fig. 9. (a) Histogram of homogenization temperatures of fluid inclusions in Sn and Sn-W deposits, with data from Naumov et al. (2011). (b) Plot of fraction of precipitated Sn and the evolving Sn isotopic composition of the precipitated Sn in a transport-precipitation model, by assuming dominance of different Sn species in the hydrothermal fluid. (c) Histogram of published Sn isotope data in cassiterite, with data from Yao et al. (2018), Wang et al. (2019a), and Mason et al. (2020). (d) Modeled Sn isotope distribution of cassiterite corresponding to species of fluid in (b).

(2005), and (2) the  $1000\ln^{122/116}\beta$  values for  $\text{SnCl}_4$ , *cis*- $\text{SnCl}_4(\text{H}_2\text{O})_2(\text{aq})$ ,  $\text{SnCl}_3^-(\text{aq})$  and cassiterite calculated at the B3LYP/TZVP level. These two models are referred to “Model-II” and “Model-III”, respectively. The  $1000\ln^{122/116}\beta$  values employed in these models are tabulated in Table S5 in the supplementary materials.

Because hydrothermal Sn deposit is commonly associated with granite magmatism (Heinrich, 1990; Lehmann, 1990; Chen et al., 2000), the  $\delta^{122/116}\text{Sn}$  of the starting hydrothermal fluid is set to be the same as that of granodiorite GSP-2, which is 0.53‰ relative to NIST 3161a (Creech et al., 2017; She et al., 2020). The transport-precipitation model (i.e., Eqs. (16) and (17)) requires a solubility function of cassiterite. Both theoretical (Jackson and

Helgeson, 1985) and experimental (Wilson and Eugster, 1990; Taylor and Wall, 1993; Schmidt, 2018) studies have consistently pointed to a strong positive temperature dependence of Sn solubility in hydrothermal fluids. When the hydrothermal fluid reaches saturation to precipitate cassiterite, the Sn concentration in fluid inclusions can be regarded as its solubility at the specific temperature recorded in the fluid inclusion. For the convenience of the following discussion, we derived a temperature-dependent function of cassiterite solubility by empirical fitting of the systematic *in situ* LA-ICP-MS data of well-characterized fluid inclusions in Audétat et al. (1998). For modeling of Sn isotope evolution during transport-precipitation, we assume that the starting hydrothermal fluid reaches satura-

tion at 500 °C (Audéat et al., 1998) and has a Sn concentration of 361 ppm. Tin mineralization was found to be mainly associated with hydrothermal fluids of 500 °C and 200 °C (Fig. 9a) (Heinrich, 1990; Naumov et al., 2011; Bodnar et al., 2014). The Sn isotope composition of the precipitated SnO<sub>2</sub> at different temperature intervals (50 °C every step) during cooling is calculated according to the equilibrium fractionation factors between hydrothermal fluids and cassiterite. The cassiterite solubility data employed in the transport-precipitation model are tabulated in Table S6 in the supplementary materials.

The results of Model-I are plotted in Fig. 9b, and the results of Model-II and Model-III are plotted in Figs. S7b and S8b in the supplementary materials. In the model, the most intense Sn precipitation occurs in the temperature bracket of 500–450 °C, and the amount of Sn precipitation decreases rapidly with decreasing temperature, a trend expected from the strong temperature dependence of Sn solubility. Because cassiterite enriches heavy Sn isotopes relative to all aqueous Sn species, the remaining hydrothermal fluid becomes isotopically light as the transport-precipitation process proceeds, and thus the  $\delta^{122/116}\text{Sn}$  of subsequent cassiterite precipitates also becomes progressively smaller. However, the trend of  $\delta^{122/116}\text{Sn}$  evolution in the model is dependent on the Sn isotope fractionation factor between aqueous fluid and cassiterite, which is controlled by the Sn speciation in the model setting. As shown in Fig. 9b, if we assume that the Sn in hydrothermal fluids occurs as Sn(IV) species (i.e., SnCl<sub>4</sub>(g), SnCl<sub>4</sub>(H<sub>2</sub>O)<sub>2</sub>(aq), SnCl<sub>6</sub><sup>2-</sup>(aq)), the model will predict a moderate decrease in  $\delta^{122/116}\text{Sn}$  of cassiterite as the transport-precipitation process goes on. For Model-II and Model-III, we obtain almost the same results (see Figs. S7b and S8b in the supplementary materials). Specifically, in Model-I, cassiterite precipitated at 200 °C would have  $\delta^{122/116}\text{Sn}$  of  $-0.56\%$ ,  $-0.98\%$ , and  $-2.15\%$ , if Sn occurs as SnCl<sub>4</sub>(g), SnCl<sub>4</sub>(H<sub>2</sub>O)<sub>2</sub>(aq), and SnCl<sub>6</sub><sup>2-</sup>(aq) in hydrothermal fluids. However, if we assume that Sn in hydrothermal fluids occurs as Sn(II) species (i.e., SnCl<sub>2</sub>(H<sub>2</sub>O)(g), SnCl<sub>2</sub>(g), SnCl<sub>2</sub>(H<sub>2</sub>O)(aq), and SnCl<sub>3</sub><sup>-</sup>(aq)), a much faster decrease in  $\delta^{122/116}\text{Sn}$  of cassiterite is predicted by the model as the hydrothermal fluid cools down during its transport, that cassiterite precipitated at 200 °C would have  $\delta^{122/116}\text{Sn}$  of  $-3.73\%$ ,  $-3.85\%$ ,  $-3.98\%$ , and  $-4.23\%$ , if Sn occurs as SnCl<sub>2</sub>(H<sub>2</sub>O)(g), SnCl<sub>2</sub>(g), SnCl<sub>2</sub>(H<sub>2</sub>O)(aq), and SnCl<sub>3</sub><sup>-</sup>(aq) in hydrothermal fluids.

The next step is to treat the results of the continuous transport-precipitation model to make them comparable with the observed Sn isotope distribution pattern in natural cassiterite. Assuming that such Sn isotope data are from randomly sampled natural cassiterite of hydrothermal origin, then sampling randomness can be approximated by fluid inclusion data in literature, as the ores host both cassiterite and quartz veins. Based on the compilation of Naumov et al. (2011) on fluid inclusion homogenization temperature for Sn mineral deposits (Fig. 9a), we can estimate the probability of sampling for cassiterite at different temperature brackets. Such probability is incorporated into a Monte Carlo simulation program coded with MATLAB that is coupled with the transport-precipitation model

described above, to derive the distribution of  $\delta^{122/116}\text{Sn}$  values of randomly sampled cassiterite. The Monte Carlo simulation was performed 10,000,000 times for each model, and the distribution pattern of  $\delta^{122/116}\text{Sn}$  for cassiterite was plotted for assumption of certain Sn species in the hydrothermal fluid. By comparing the predicted distribution pattern of  $\delta^{122/116}\text{Sn}$  of cassiterite based on modeling (Fig. 9d) and that of measured from natural samples (Fig. 9c), it is clear that only models treating aqueous Sn as Sn(IV) species can reproduce the  $\delta^{122/116}\text{Sn}$  pattern of natural cassiterite well. If Sn solely occurs as Sn(II) species in hydrothermal fluids during cassiterite mineralization, a much larger range in  $\delta^{122/116}\text{Sn}$  would be expected from natural cassiterite. The conclusion also holds true for Model-II and Model-III (as shown in Figs. S7d and S8d in the supplementary materials, respectively). Therefore, we suggest that during tin mineralization in hydrothermal systems, Sn in hydrothermal fluids should have occurred as Sn(IV) species.

Sn<sup>4+</sup> plays an important role in various geological processes. Sn<sup>4+</sup> dominates over Sn<sup>2+</sup> in terrestrial magmatic systems (Badullovich et al., 2017). Sn occurs in minerals such as biotite, titanite, rutile, and magnetite by substitution of Sn<sup>4+</sup> for Ti<sup>4+</sup> or Fe<sup>3+</sup> (e.g., Schwartz et al., 1995; Wang et al., 2017; Durasova et al., 1986; Liu et al., 2016). During hydrothermal alteration igneous rocks, Sn<sup>4+</sup> in these minerals are broken down and released into the fluid (e.g., Johan and Johan, 2005; Zhao et al., 2005; Wang et al., 2013). Schmidt (2018) had strongly argued that the role of Sn(IV) species during tin hydrothermal mineralization might have been significantly more important than previously thought, and our modeling results are consistent with this viewpoint.

However, numerous previous studies did report stability of Sn(II) species under hydrothermal conditions (e.g., Pabalan, 1986; Wilson and Eugster, 1990; Taylor and Wall, 1993; Sherman et al., 2000; Müller and Seward, 2001; Duc-Tin et al., 2007). If Sn(II) species had existed in tin mineralization systems, an increase in redox state of Sn (from Sn<sup>2+</sup> to Sn<sup>4+</sup>) prior to its precipitation needs to be incurred, and such redox change could occur immediately after fluid exsolution from magma, or at the very early stage of fluid transport in the hydrothermal system. Finally, we note that the modeling in Fig. 9 assumes cassiterite precipitation is driven by temperature decrease. If the cassiterite precipitation process is associated with other processes such as boiling, liquid–vapor Sn isotope fractionation will complicate the scenario and allow for the existence of redox reactions during precipitation. Hence, we do not completely rule out the role of Sn(II) for tin mineralization and we do not deny the importance of redox reactions in tin deposits as proposed in Yao et al. (2018). Instead, both Yao et al. (2018) and this study highlighted the usefulness of Sn stable isotopes in deepening our understanding of Sn mineral deposits.

## 5. CONCLUSIONS

In this study, by using first principles simulations, we investigated the speciation and stability of Sn(II)—Cl spe-

cies in hydrothermal fluids, and calculated the equilibrium Sn isotope fractionation factors of dominant species as well as Sn-bearing minerals (cassiterite, megawite, and romarchite). The following Sn(II)—Cl species have been found to be stable:  $\text{SnCl}_3^-$ ,  $\text{SnCl}_2(\text{H}_2\text{O})$ , and  $\text{SnCl}(\text{H}_2\text{O})_2^+$  in aqueous solutions with  $\text{SnCl}_3^-$  dominating,  $\text{SnCl}_2$  and  $\text{SnCl}_2(\text{H}_2\text{O})$  in vapor phases, and  $\text{SnCl}_2$  in supercritical aqueous fluids.  $\text{SnCl}_4^{2-}$  has low stability even at ambient conditions and it is unstable at elevated temperatures. The calculated equilibrium Sn isotope fractionation factors indicated that heavy Sn isotopes tend to concentrate in high valence species and minerals, and gaseous species enrich heavy Sn isotopes over aqueous species. Based on the calculated equilibrium isotope fractionation factors, we evaluated the isotopic effect of Sn speciation on cassiterite precipitation by a transport-precipitation model coupled with Monte Carlo simulation, and found that only when Sn (IV) species are considered in the model, the modeling results can match Sn isotope data measured from natural cassiterite. Based on these, we reasoned that Sn occurs as Sn(IV) species in hydrothermal mineralization systems for cassiterite. As such, the derived speciation, molecular level structures and equilibrium isotope fractionation factors provide a basis for future studies on the properties and behaviors of Sn in various geochemical processes.

### Declaration of Competing Interest

The authors declare that they have no known competing financial interests or personal relationships that could have appeared to influence the work reported in this paper.

### ACKNOWLEDGEMENT

This study was supported by the National Key R&D Program of China (No. 2018YFA0702700), the National Natural Science Foundation of China (No. 41872041 to X. Liu, No. 41622301 to W. Li, and 92062213 to X. Lu), the China Postdoctoral Science Foundation (No. 2019M651778), the Fundamental Research Funds for the Central Universities (No. XJ2020003101), and the Graduate Scientific Research Innovation Program of Jiangsu Province (No. KYCX20\_0044). We acknowledge the financial support from the State Key Laboratory for Mineral Deposits Research at Nanjing University. We are grateful to the High Performance Computing Center (HPCC) of Nanjing University for doing the numerical calculations in this paper on its blade cluster system. We thank Prof. Christoph A. Heinrich and Dr. Andreas Audétat for their generous help on providing microthermometry data and useful suggestion. This study benefited from constructive comments from R. Mathur and two anonymous reviewers, as well as comments from associate editor Marc Blanchard.

### APPENDIX A. SUPPLEMENTARY MATERIAL

Supplementary data to this article can be found online at <https://doi.org/10.1016/j.gca.2021.02.023>.

### REFERENCES

Altunay N. and Gürkan R. (2015) An inexpensive and sensitive method for speciative determination of Sn(IV), Sn(II), and total

- Sn as Sn(IV) in selected beverages by micellar improved spectrophotometry. *Food Anal. Methods* **8**, 994–1004.
- Audétat A., Günther D. and Heinrich C. A. (1998) Formation of a magmatic-hydrothermal ore deposit: insights with LA-ICP-MS analysis of fluid inclusions. *Science* **279**, 2091–2094.
- Badullovich N., Moynier F., Creech J., Teng F.-Z. and Sossi P. A. (2017) Tin isotopic fractionation during igneous differentiation and Earth's mantle composition. *Geochem. Persp. Lett.* **5**, 24–28.
- Balliana E., Aramendía M., Resano M., Barbante C. and Vanhaecke F. (2013) Copper and tin isotopic analysis of ancient bronzes for archaeological investigation: development and validation of a suitable analytical methodology. *Anal. Bioanal. Chem.* **405**, 2973–2986.
- Becke A. D. (1993) Density-functional thermochemistry. III. The role of exact exchange. *J. Chem. Phys.* **98**, 5648–5652.
- Bhalla P., Holtz F., Linnen R. L. and Behrens H. (2005) Solubility of cassiterite in evolved granitic melts: effect of  $T$ ,  $f\text{O}_2$ , and additional volatiles. *Lithos* **80**, 387–400.
- Bigeleisen J. and Mayer M. G. (1947) Calculation of equilibrium constants for isotopic exchange reactions. *J. Chem. Phys.* **15**, 261–267.
- Blanchard M., Balan E. and Schauble E. A. (2017) Equilibrium fractionation of non-traditional isotopes: a molecular modeling perspective. *Rev. Mineral. Geochem.* **82**, 27–63.
- Bodnar, R.J., Lecumberri-Sanchez, P., Moncada, D., Steele-MacInnis, M., 2014. Fluid inclusions in hydrothermal ore deposits. In: Scott, S.D. (Ed.), *Treatise on Geochemistry*, 2nd ed. vol. 13. Elsevier Science, pp. 119–142.
- Bolzan A. A., Fong C., Kennedy B. J. and Howard C. J. (1997) Structural studies of rutile-type metal dioxides. *Acta Cryst. B* **53**, 373–380.
- Brugger J., Liu W., Etschmann B., Mei Y., Sherman D. M. and Testemale D. (2016) A review of the coordination chemistry of hydrothermal systems, or do coordination changes make ore deposits?. *Chem. Geol.* **447** 219–253.
- Byrd R. H., Lu P., Nocedal J. and Zhu C. (1995) A limited memory algorithm for bound constrained optimization. *SIAM J. Sci. Comput.* **16**, 1190–1208.
- Carter E. A., Ciccotti G., Hynes J. T. and Kapral R. (1989) Constrained reaction coordinate dynamics for the simulation of rare events. *Chem. Phys. Lett.* **156**, 472–477.
- Chen J., Wang R., Zhou J. and Ji J. (2000) *Geochemistry of Tin*. Nanjing University Press (in Chinese).
- Creech J. B. and Moynier F. (2019) Tin and zinc stable isotope characterisation of chondrites and implications for early Solar System evolution. *Chem. Geol.* **511**, 81–90.
- Creech J. B., Moynier F. and Badullovich N. (2017) Tin stable isotope analysis of geological materials by double-spike MCICPMS. *Chem. Geol.* **457**, 61–67.
- Davico G. E., Ramond T. M. and Lineberger W. C. (2000) Photoelectron spectroscopy of SnO. *J. Chem. Phys.* **113**, 8852.
- de Lima Batista A. P., de Lima J. C. B., Franzreb K. and Ornellas F. R. (2012) A theoretical study of  $\text{SnF}^{2+}$ ,  $\text{SnCl}^{2+}$ , and  $\text{SnO}^{2+}$  and their experimental search. *J. Chem. Phys.* **137**, 154302.
- Duc-Tin Q., Audétat A. and Keppler H. (2007) Solubility of tin in (Cl, F)-bearing aqueous fluids at 700 °C, 140 MPa: a LA-ICP-MS study on synthetic fluid inclusions. *Geochim. Cosmochim. Acta* **71**, 3323–3335.
- Durasova N. A., Ryabchikov I. D. and Barsukov V. L. (1986) The redox potential and the behavior of tin in magmatic systems. *Int. Geol. Rev.* **28**, 305–311.
- Ermakov K. V., Butayev B. S. and Spiridonov V. P. (1991) Application of Schwinger perturbation theory in electron diffraction analysis Part II. Bent  $\text{XY}_2$ -type molecules. *J. Mol. Struct.* **248**, 143–154.

- Farges F., Linnen R. L. and Brown, Jr., G. E. (2006) Redox and speciation of tin in hydrous silicate glasses: a comparison with Nb, Ta, Mo and W. *Can. Mineral.* **44**, 795–810.
- Fields M., Devonshire R., Edwards H. G. M. and Fawcett V. (1995) Laser-Raman spectroscopic study of the vapour phase equilibria above molten SnCl<sub>2</sub>. *Spectrochim. Acta, Part A* **51**, 2249–2265.
- Foresman J. B. and Frisch A. E. (2015) *Exploring Chemistry with Electronic Structure Methods*, third ed. Gaussian Inc..
- Frisch M. J., Trucks G. W. and Schlegel H. B., et al. (2013) *Gaussian 09, Revision D.01*. Gaussian, Inc..
- Gajda T., Sipos P. and Gamsjäger H. (2009) The standard electrode potential of the Sn<sup>4+</sup>/Sn<sup>2+</sup> couple revisited. *Monatsh. Chem.* **140**, 1293–1303.
- Goedecker S., Teter M. and Hutter J. (1996) Separable dual-space Gaussian pseudopotentials. *Phys. Rev. B* **54**, 1703–1710.
- Grimme S., Antony J., Ehrlich S. and Krieg H. (2010) A consistent and accurate *ab initio* parametrization of density functional dispersion correction (DFT-D) for the 94 elements H-Pu. *J. Chem. Phys.* **132**, 154104.
- Grimme S. (2011) Density functional theory with London dispersion corrections. *Wiley Interdiscip. Rev. Comput. Mol. Sci.* **1**, 211–228.
- Guan Q., Mei Y., Etschmann B., Testemale D., Louvel M. and Brugger J. (2020) Yttrium complexation and hydration in chloride-rich hydrothermal fluids: a combined *ab initio* molecular dynamics and *in situ* X-ray absorption spectroscopy study. *Geochim. Cosmochim. Acta* **281**, 168–189.
- Guidon M., Hutter J. and VandeVondele J. (2010) Auxiliary density matrix methods for Hartree-Fock exchange calculations. *J. Chem. Theory Comput.* **6**, 2348–2364.
- Hayes S. M. and McCullough E. A. (2018) Critical minerals: a review of elemental trends in comprehensive criticality studies. *Resour. Policy* **59**, 192–199.
- Heinrich C. A. and Eadington P. J. (1986) Thermodynamic predictions of the hydrothermal chemistry of arsenic, and their significance for the paragenetic sequence of some cassiterite-arsenopyrite-base metal sulfide deposits. *Econ. Geol.* **81**, 511–529.
- Heinrich C. A. (1990) The chemistry of hydrothermal tin(-tungsten) ore deposition. *Econ. Geol.* **85**, 457–481.
- Hill P. S. and Schauble E. A. (2008) Modeling the effects of bond environment on equilibrium iron isotope fractionation in ferric aquo-chloro complexes. *Geochim. Cosmochim. Acta* **72**, 1939–1958.
- Hoover W. G. (1985) Canonical dynamics: equilibrium phase-space distributions. *Phys. Rev. A* **31**, 1695–1697.
- Huang F., Chen L., Wu Z. and Wang W. (2013) First-principles calculations of equilibrium Mg isotope fractionations between garnet, clinopyroxene, orthopyroxene, and olivine: implications for Mg isotope thermometry. *Earth Planet. Sci. Lett.* **367**, 61–70.
- Hutter J., Iannuzzi M., Schiffmann F. and VandeVondele J. (2014) CP2K: atomistic simulations of condensed matter systems. *Wiley Interdiscip. Rev. Comput. Mol. Sci.* **4**, 15–25.
- Jackson K. J. and Helgeson H. C. (1985) Chemical and thermodynamic constraints on the hydrothermal transport and deposition of tin: I. Calculation of the solubility of cassiterite at high pressures and temperatures. *Geochim. Cosmochim. Acta* **49**, 1–22.
- Jahn S., Dubrail J. and Wilke M. (2015) Complexation of Zr and Hf monomers in supercritical aqueous solutions: insights from *ab initio* molecular dynamics simulations. *Chem. Geol.* **418**, 30–39.
- Johan Z. and Johan V. (2005) Accessory minerals of the Cínovec (Zinnwald) granite cupola, Czech Republic: indicators of petrogenetic evolution. *Mineral. Petrol.* **83**, 113–150.
- Johansson G. and Ohtaki H. (1973) An X-ray investigation of the hydrolysis products of tin(II) in solution. *Acta Chem. Scand.* **27**, 643–660.
- Kalugina Y. N. and Thakkar A. J. (2015) Electric properties of stannous and stannic halides: how good are the experimental values? *Chem. Phys. Lett.* **626**, 69–72.
- Kühne T. D., Iannuzzi M. and Del Ben M., et al. (2020) CP2K: an electronic structure and molecular dynamics software package - Quickstep: efficient and accurate electronic structure calculations. *J. Chem. Phys.* **152**, 194103.
- Lee C., Yang W. and Parr R. G. (1988) Development of the Colle-Salvetti correlation-energy formula into a functional of the electron-density. *Phys. Rev. B* **37**, 785–789.
- Lee E. P. F., Dyke J. M., Mok D. K. W., Chow W.-K. and Chau F.-T. (2007) *Ab initio* calculations on SnCl<sub>2</sub> and Franck-Condon factor simulations of its *a-X* and *B-X* absorption and single-vibronic-level emission spectra. *J. Chem. Phys.* **127**, 024308.
- Lehmann B. (1990) *Metallogeny of Tin*. Springer-Verlag.
- Levy J. B., Jancsó G. and Hargittai M. (2003) Structure and thermodynamics of the tin dichloride dimer - a computational study. *J. Phys. Chem. A* **107**, 10450–10455.
- Li W., Jackson S. E., Pearson N. J. and Graham S. (2010) Copper isotopic zonation in the Northparkes porphyry Cu-Au deposit, SE Australia. *Geochim. Cosmochim. Acta* **74**, 4078–4096.
- Li X., Zhao H., Tang M. and Liu Y. (2009) Theoretical prediction for several important equilibrium Ge isotope fractionation factors and geological implications. *Earth Planet. Sci. Lett.* **287**, 1–11.
- Li X. and Liu Y. (2011) Equilibrium Se isotope fractionation parameters: a first-principles study. *Earth Planet. Sci. Lett.* **304**, 113–120.
- Lippert G., Hutter J. and Parrinello M. (1997) A hybrid Gaussian and plane wave density functional scheme. *Mol. Phys.* **92**, 477–487.
- Liu X., Lu X., Wang R. and Zhou H. (2012) Silver speciation in chloride-containing hydrothermal solutions from first principles molecular dynamics simulations. *Chem. Geol.* **294–295**, 103–112.
- Liu X., Vinograd V. L., Lu X., Leonenko E. V., Eremin N. N., Wang R. and Winkler B. (2016) Thermodynamics of mixing in an isostructural solid solution: simulation methodologies and application to the rutile-cassiterite system. *Am. Mineral.* **101**, 1197–1206.
- Liu Y. and Tossell J. A. (2005) *Ab initio* molecular orbital calculations for boron isotope fractionations on boric acids and borates. *Geochim. Cosmochim. Acta* **69**, 3995–4006.
- Malinovskiy D., Moens L. and Vanhaecke F. (2009) Isotopic fractionation of Sn during methylation and demethylation reactions in aqueous solution. *Environ. Sci. Technol.* **43**, 4399–4404.
- Martyna G. J. and Tuckerman M. E. (1999) A reciprocal space based method for treating long range interactions in *ab initio* and force-field-based calculations in clusters. *J. Chem. Phys.* **110**, 2810–2821.
- Mason A. H., Powell W. G., Bankoff H. A., Mathur R., Bulatović A., Filipović V. and Ruiz J. (2016) Tin isotope characterization of bronze artifacts of the central Balkans. *J. Archaeol. Sci.* **69**, 110–117.
- Mason A., Powell W., Bankoff H. A., Mathur R., Price M., Bulatović A. and Filipović V. (2020) Provenance of tin in the Late Bronze Age balkans based on probabilistic and spatial analysis of Sn isotopes. *J. Archaeol. Sci.* **122**, 105–181.
- McQuarrie D. A. and Simon J. D. (1999) *Molecular Thermodynamics*. University Science Books.
- Méheut M. and Schauble E. A. (2014) Silicon isotope fractionation in silicate minerals: insights from first-principles models of

- phyllosilicates, albite and pyrope. *Geochim. Cosmochim. Acta* **134**, 137–154.
- Méheut M., Ibáñez-Mejía M. and Tissot F. L. H. (2021) Drivers of zirconium isotope fractionation in Zr-bearing phases and melts: the roles of vibrational, nuclear field shift and diffusive effects. *Geochim. Cosmochim. Acta* **292**, 217–234.
- Mei Y., Sherman D. M., Liu W. and Brugger J. (2013) *Ab initio* molecular dynamics simulation and free energy exploration of copper(I) complexation by chloride and bisulfide in hydrothermal fluids. *Geochim. Cosmochim. Acta* **102**, 45–64.
- Mei Y., Liu W., Sherman D. M. and Brugger J. (2014) Metal complexation and ion hydration in low density hydrothermal fluids: *ab initio* molecular dynamics simulation of Cu(I) and Au (I) in chloride solutions (25–1000 °C, 1–5000 bar). *Geochim. Cosmochim. Acta* **131**, 196–212.
- Müller B. and Seward T. M. (2001) Spectrophotometric determination of the stability of tin(II) chloride complexes in aqueous solution up to 300°C. *Geochim. Cosmochim. Acta* **65**, 4187–4199.
- Müller B., Frischknecht R., Seward T., Heinrich C. and Gallegos W. C. (2001) A fluid inclusion reconnaissance study of the Huanuni tin deposit (Bolivia), using LA-ICP-MS micro-analysis. *Mineral. Deposita* **36**, 680–688.
- Naumov V. B., Dorofeev V. A. and Mironova O. F. (2011) Physicochemical parameters of the formation of hydrothermal deposits: a fluid inclusion study. I. Tin and tungsten deposits. *Geochem. Int.* **49**, 1002–1021.
- Nosé S. (1984a) A molecular dynamics method for simulations in the canonical ensemble. *Mol. Phys.* **52**, 255–268.
- Nosé S. (1984b) A unified formulation of the constant temperature molecular dynamics methods. *J. Chem. Phys.* **81**, 511–519.
- Pabalan, R.T., 1986. Solubility of cassiterite (SnO<sub>2</sub>) in NaCl solutions from 200°C–350°C, with geologic applications. Ph.D. thesis. Pennsylvania State University.
- Pannetier J. and Denes G. (1980) Tin(II) oxide: structure refinement and thermal expansion. *Acta Cryst. B* **36**, 2763–2765.
- Pavlova G. G., Palesky S. V., Borisenko A. S., Vladimirov A. G., Seifert T. and Phan L. A. (2015) Indium in cassiterite and ores of tin deposits. *Ore Geol. Rev.* **66**, 99–113.
- Perdew J. P., Burke K. and Ernzerhof M. (1996) Generalized gradient approximation made simple. *Phys. Rev. Lett.* **77**, 3865–3868.
- Perdew J. P. and Ruzsinszky A. (2010) Density functional theory of electronic structure: a short course for mineralogists and geophysicists. *Rev. Mineral. Geochem.* **71**, 1–18.
- Persson L., D'Angelo P. and Lundberg D. (2016) Hydrated and solvated tin(II) ions in solution and the solid state, and a coordination chemistry overview of the d<sup>10</sup>s<sup>2</sup> metal ions. *Chem. Eur. J.* **22**, 18583–18592.
- Peterson K. A. (2003) Systematically convergent basis sets with relativistic pseudopotentials. I. Correlation consistent basis sets for the post-d group 13–15 elements. *J. Chem. Phys.* **119**, 11099–11112.
- Pokrovski G. S., Borisova A. Y. and Bychkov A. Y. (2013a) Speciation and transport of metals and metalloids in geological vapors. *Rev. Mineral. Geochem.* **76**, 165–218.
- Pokrovski G. S., Roux J., Ferlat G., Jonchiere R., Seitsonen A. P., Vuilleumier R. and Hazemann J.-L. (2013b) Silver in geological fluids from in situ X-ray absorption spectroscopy and first-principles molecular dynamics. *Geochim. Cosmochim. Acta* **106**, 501–523.
- Polyakov V. B., Mineev S. D., Clayton R. N., Hu G. and Mineev K. S. (2005) Determination of tin equilibrium isotope fractionation factors from synchrotron radiation experiments. *Geochim. Cosmochim. Acta* **69**, 5531–5536.
- Qin T., Wu F., Wu Z. and Huang F. (2016) First-principles calculations of equilibrium fractionation of O and Si isotopes in quartz, albite, anorthite, and zircon. *Contrib. Mineral. Petrol.* **171**, 91.
- Qu Q., Liu G., Henry M., Point D., Chmieleff J., Sun R., Sonke J. E. and Chen J. (2020) Tin stable isotopes in magmatic-affected coal deposits: insights in the geochemical behavior of tin. *Appl. Geochem.* **119**, 104641.
- Raghavachari K., Trucks G. W., Pople J. A. and Head-Gordon M. (1989) A fifth-order perturbation comparison of electron correlation theories. *Chem. Phys. Lett.* **157**, 479–483.
- Roskosz M., Amet Q., Fitoussi C., Dauphas N., Bourdon B., Tissandier L., Hu M. Y., Said A., Alatas A. and Alp E. E. (2020) Redox and structural controls on tin isotopic fractionations among magmas. *Geochim. Cosmochim. Acta* **268**, 42–55.
- Rustad J. R., Nelmes S. L., Jackson V. E. and Dixon D. A. (2008) Quantum-chemical calculations of carbon-isotope fractionation in CO<sub>2</sub>(g), aqueous carbonate species, and carbonate minerals. *J. Phys. Chem. A* **112**, 542–555.
- Schauble E. A. (2004) Applying stable isotope fractionation theory to new systems. *Rev. Mineral. Geochem.* **55**, 65–111.
- Schauble E. A. (2011) First-principles estimates of equilibrium magnesium isotope fractionation in silicate, oxide, carbonate and hexaaquamagnesium(2+) crystals. *Geochim. Cosmochim. Acta* **75**, 844–869.
- Schmidt C. (2018) Formation of hydrothermal tin deposits: Raman spectroscopic evidence for an important role of aqueous Sn(IV) species. *Geochim. Cosmochim. Acta* **220**, 499–511.
- Schwartz M. O., Rajah S. S., Askury A. K., Putthapiban P. and Djaswadi S. (1995) The Southeast Asian tin belt. *Earth Sci. Rev.* **38**, 95–293.
- She J.-X., Wang T., Liang H., Muhtar M. N., Li W. and Liu X. (2020) Sn isotope fractionation during volatilization of Sn (IV) chloride: laboratory experiments and quantum mechanical calculations. *Geochim. Cosmochim. Acta* **269**, 184–202.
- Sherman D. M., Ragnarsdottir K. V., Oelkers E. H. and Collins C. R. (2000) Speciation of tin (Sn<sup>2+</sup> and Sn<sup>4+</sup>) in aqueous Cl solutions from 25°C to 350°C: an in situ EXAFS study. *Chem. Geol.* **167**, 169–176.
- Sherman D. M. (2007) Complexation of Cu<sup>+</sup> in hydrothermal NaCl brines: *ab initio* molecular dynamics and energetics. *Geochim. Cosmochim. Acta* **71**, 714–722.
- Sherman D. M. (2010) Metal complexation and ion association in hydrothermal fluids: insights from quantum chemistry and molecular dynamics. *Geofluids* **10**, 41–57.
- Sprik M. and Ciccotti G. (1998) Free energy from constrained molecular dynamics. *J. Chem. Phys.* **109**, 7737–7744.
- Stefanski J. and Jahn S. (2020) Yttrium speciation in subduction-zone fluids from *ab initio* molecular dynamics simulations. *Solid Earth* **11**, 767–789.
- Sverjensky D. A., Harrison B. and Azzolini D. (2014) Water in the deep Earth: the dielectric constant and the solubilities of quartz and corundum to 60 kb and 1200 °C. *Geochim. Cosmochim. Acta* **129**, 125–145.
- Tarselli M. A. (2017) Tin can. *Nature Chem.* **9**, 500.
- Taylor J. R. and Wall V. J. (1993) Cassiterite solubility, tin speciation, and transport in a magmatic aqueous phase. *Econ. Geol.* **88**, 437–460.
- Teng F.-Z., Dauphas N. and Watkins J. M. (2017) Non-traditional stable isotopes: retrospective and prospective. *Rev. Mineral. Geochem.* **82**, 1–26.
- Thanthirivatte K. S., Vasiliu M., Battey S. R., Lu Q., Peterson K. A., Andrews L. and Dixon D. A. (2015) Gas phase properties of MX<sub>2</sub> and MX<sub>4</sub> (X = F, Cl) for M = group 4, group 14, cerium, and thorium. *J. Phys. Chem. A* **119**, 5790–5803.

- Togo A. and Tanaka I. (2015) First principles phonon calculations in materials science. *Scr. Mater.* **108**, 1–5.
- Urey H. C. (1947) The thermodynamic properties of isotopic substances. *J. Chem. Soc.*, 562–581.
- VandeVondele J., Mohamed F., Krack M., Hutter J., Sprik M. and Parrinello M. (2005a) The influence of temperature and density functional models in *ab initio* molecular dynamics simulation of liquid water. *J. Chem. Phys.* **122**, 014515.
- VandeVondele J., Krack M., Mohamed F., Parrinello M., Chas-saing T. and Hutter J. (2005b) QUICKSTEP: Fast and accurate density functional calculations using a mixed Gaussian and plane waves approach. *Comput. Phys. Commun.* **167**, 103–128.
- VandeVondele J. and Hutter J. (2007) Gaussian basis sets for accurate calculations on molecular systems in gas and condensed phases. *J. Chem. Phys.* **127**, 114105.
- Wagner W., Cooper J. R., Dittmann A., Kijima J., Kretzschmar H.-J., Kruse A., Mareš R., Oguchi K., Sato H., Stöcker I., Šifner O., Takaishi Y., Tanishita I., Trübenbach J. and Willkommen T. (2000) The IAPWS industrial formulation 1997 for the thermodynamic properties of water and steam. *J. Eng. Gas Turbines Power.* **122**, 150–184.
- Wagner J., Haigis V., Künzel D. and Jahn S. (2017a) Trace element partitioning between silicate melts - a molecular dynamics approach. *Geochim. Cosmochim. Acta* **205**, 245–255.
- Wagner J., Haigis V., Leydier M., Bytchkov A., Cristiglio V., Fischer H. E., Sadiki N., Zanghi D., Hennem L. and Jahn S. (2017b) The structure of Y- and La-bearing aluminosilicate glasses and melts: a combined molecular dynamics and diffraction study. *Chem. Geol.* **461**, 23–33.
- Wang D., Mathur R., Powell W., Godfrey L. and Zheng Y. (2019a) Experimental evidence for fractionation of tin chlorides by redox and vapor mechanisms. *Geochim. Cosmochim. Acta* **250**, 209–218.
- Wang R. C., Xie L., Chen J., Yu A., Wang L., Lu J. and Zhu J. (2013) Tin-carrier minerals in metaluminous granites of the western Nanling Range (southern China): constraints on processes of tin mineralization in oxidized granites. *J. Asian Earth Sci.* **74**, 361–372.
- Wang R. C., Xie L., Lu J. J., Zhu J. C. and Chen J. (2017) Diversity of Mesozoic tin-bearing granites in the Nanling and adjacent regions, South China: distinctive mineralogical patterns. *Sci. China Earth Sci.* **60**, 1909–1919.
- Wang T., Liu X., Sun Y., Lu X. and Wang R. (2020) Coordination of  $Zr^{4+}/Hf^{4+}/Nb^{5+}/Ta^{5+}$  in silicate melts: insight from first principles molecular dynamics simulations. *Chem. Geol.* **555**, 119814.
- Wang X., Amet Q., Fitoussi C. and Bourdon B. (2018) Tin isotope fractionation during magmatic processes and the isotope composition of the bulk silicate Earth. *Geochim. Cosmochim. Acta* **228**, 320–335.
- Wang X., Fitoussi C., Bourdon B., Fegley, Jr., B. and Charnoz S. (2019b) Tin isotopes indicative of liquid-vapour equilibration and separation in the Moon-forming disk. *Nat. Geosci.* **12**, 707–711.
- Weigend F. and Ahlrichs R. (2005) Balanced basis sets of split valence, triple zeta valence and quadruple zeta valence quality for H to Rn: design and assessment of accuracy. *Phys. Chem. Chem. Phys.* **7**, 3297–3305.
- Wentzcovitch R. M., Yu Y. G. and Wu Z. (2010) Thermodynamic properties and phase relations in mantle minerals investigated by first principles quasiharmonic theory. *Rev. Mineral. Geochem.* **71**, 59–98.
- Wilson, G.A., Eugster, H.P., 1990. Cassiterite solubility and tin speciation in supercritical chloride solutions. In: Spencer, R.J., Chou, I.-M. (Eds.), Fluid-Mineral Interactions: A Tribute to H. P. Eugster. The Geochemical Society, Special Publication No. 2, pp. 179–195.
- Wolf A., Reiher M. and Hess B. A. (2004) Correlated *ab initio* calculations of spectroscopic parameters of SnO within the framework of the higher-order generalized Douglas-Kroll transformation. *J. Chem. Phys.* **120**, 8624.
- Woon D. E. and Dunning, Jr., T. H. (1993) Gaussian basis sets for use in correlated molecular calculations. III. The atoms aluminum through argon. *J. Chem. Phys.* **98**, 1358–1371.
- Wu F., Qin T., Li X., Liu Y., Huang J.-H., Wu Z. and Huang F. (2015a) First-principles investigation of vanadium isotope fractionation in solution and during adsorption. *Earth Planet. Sci. Lett.* **426**, 216–224.
- Wu Z., Huang F. and Huang S. (2015b) Isotope fractionation induced by phase transformation: first-principles investigation for  $Mg_2SiO_4$ . *Earth Planet. Sci. Lett.* **409**, 339–347.
- Wu Z. Q. and Wang W. Z. (2016) First-principles calculations of elasticity of minerals at high temperature and pressure. *Sci. China Earth Sci.* **59**, 1107–1137.
- Yamaguchi T., Lindqvist O., Claesson T. and Boyce J. B. (1982) EXAFS and X-ray diffraction studies of the hydration structure of stereochemically active Sn(II) ions in aqueous solution. *Chem. Phys. Lett.* **93**, 528–532.
- Yao J., Mathur R., Powell W., Lehmann B., Tornos F., Wilson M. and Ruiz J. (2018) Sn-isotope fractionation as a record of hydrothermal redox reactions. *Am. Mineral.* **103**, 1591–1598.
- Zhang Z. and Duan Z. (2005) Prediction of the PVT properties of water over wide range of temperatures and pressures from molecular dynamics simulation. *Phys. Earth Planet. Inter.* **149**, 335–354.
- Zhang Z., Mao Z., Liu X., Zhang Y. and Brodholt J. (2018) Stability and reactions of  $CaCO_3$  polymorphs in the Earth's deep mantle. *J. Geophys. Res. Solid Earth* **123**, 6491–6500.
- Zhao J., Ross N. L. and Angel R. J. (2004) Tilting and distortion of  $CaSnO_3$  perovskite to 7 GPa determined from single-crystal X-ray diffraction. *Phys. Chem. Minerals* **31**, 299–305.
- Zhao K.-D., Jiang S.-Y., Jiang Y.-H. and Wang R.-C. (2005) Mineral chemistry of the Qitianling granitoid and the Furong tin oredeposit in Hunan Province, South China: implication for the genesis of granite and related tin mineralization. *Eur. J. Mineral.* **17**, 635–648.

Associate editor: Marc Blanchard